12-2019

Investigation of a Candidate for Cosmic Ray Acceleration

Jordan Lynn Eagle
Clemson University, jeagle@radford.edu

Investigation of a Candidate for Cosmic Ray Acceleration

A Thesis
Presented to
the Graduate School of
Clemson University

In Partial Fulfillment
of the Requirements for the Degree
Master of Science
Physics

---

by
Jordan L. Eagle
December 2019

Accepted by:
Dr. Marco Ajello, Committee Chair
Dr. Mark Leising
Dr. Dieter Hartmann

Abstract

Studies of the non-thermal Galactic source population are essential to understand how and where the bulk of cosmic rays are being accelerated and to understand the mechanisms underlying very high energy (VHE, E>50 GeV) emitters [39, 51]. The plane of the Milky Way is rich with supernova remnants (SNRs) and pulsar wind nebulae (PWNe) which are efficient accelerators of cosmic rays (CRs) - whose interaction with the surrounding photon fields produces energetic γ-rays and neutrinos. SNRs and PWNe are some of the most powerful objects in our Galaxy and because they emit at very high energies (VHE, E>50 GeV), γ-rays represent an excellent probe of the non-thermal astrophysical processes in these objects.

Relativistic electrons (i.e. leptons) can produce γ-rays by non-thermal bremsstrahlung or by inverse Compton scattering (IC) on ambient photon fields, whereas protons and heavier nuclei (i.e. hadrons) can generate γ-rays by the process of pion decay, produced in collisions between relativistic hadrons and ambient material. Understanding the particle population responsible for the observed γ-ray emission can provide clues to the potential of CR acceleration as most cosmic rays are made of protons or heavier nuclei ($\sim$10% of all cosmic rays are leptons) so, if it can be established that the γ-ray emission is hadronic in origin, then we can better understand the likelihood for hadron CR acceleration in VHE objects.

In this thesis, we report on the investigation of a very high energy (VHE), Galactic γ-ray source recently discovered at >50 GeV using the Large Area Telescope (LAT) on board *Fermi*. This object, 2FHL J0826.1−4500, displays one of the hardest >50 GeV spectra ($\Gamma_\gamma \sim 1.6$) in the 2FHL sample, and a follow-up observation with XMM-*Newton* has uncovered diffuse, soft thermal emission at the position of the γ-ray source. A detailed analysis of the available multi-wavelength data shows that this source is located on the Western edge of the Vela supernova remnant: the observations and the spectral energy distribution modeling support a scenario where this γ-ray source is the

byproduct of the interaction between the SNR shock and a neutral Hydrogen cloud. If confirmed, this shock-cloud interaction would make 2FHL J0826.1−4500 a promising candidate for efficient particle acceleration. This work has been recently published in the Astrophysical Journal [30].

In chapter 1, the objective of this thesis is introduced. In chapter 2, SNRs and PWNe are explained in detail with a focus on the Vela SNR - the closest composite SNR to Earth. In chapter 3, we discuss the main instruments used to obtain the γ-ray and X-ray data, namely XMM-*Newton* and the *Fermi*-LAT. Chapter 4 describes the data reduction process and spectral analysis and a multi-wavelength description of 2FHL J0826.1−4500 is presented in chapter 5. Chapter 6 tests the spectral energy distribution (SED) of the source, attempting to determine the dominant parent particle population to better understand its emission mechanisms. In chapter 7 we report our conclusions on 2FHL J0826.1−4500 and emphasize important properties that still need to be probed in order to best answer the underlying question: if 2FHL J0826.1−4500 is an efficient particle accelerator, can we safely establish if this is a site generating fresh CRs or does the energetic environment favor a scenario where pre-existing CRs are being re-accelerated here?

Dedication

Warning: This section of my thesis is going to be very emotional and possibly cheesy.

This work is dedicated to my family: my mom (Jeannie Eagle), my father (John Eagle), and my sister (Jamie Elkhill). These people have seen my bests and my worsts since I've been a living, breathing human being. Clearly, they deserve to own a part of this glory with me. Let me also be a little silly and dedicate this to my animals as well: Ruca, my Beagle, and Mars, my tabby cat. They are very special animals that have been cute, adorable, and loving, even in my darkest of hours. In fact, let's dedicate this to all animals everywhere - thanks for dealing with humans. This one's for you.

Back to being serious, I need to emphasize two very special people who 100% are responsible for my even being capable of getting to this point: My father and grandfather (Jim Eagle). To my father, for instilling my sense of wonder in the stars from a small age. For exposing me to the movie *Contact* (and then later, the book). To this day, I will tell anyone that this movie has a significant impact on my initial decision in choosing physics. Seriously though, Dad, you have been a grand influence in my life and I love you so much!

To Jim Eagle, my grandfather, who unfortunately passed away just last year on May, 29, 2018. For your intellect, advice, love, support, and also for raising such an amazing son that I get to call Dad. We argued and discussed politics and science often and even though we may have had wildly different views on some topics, your insight was invaluable. You were well-read and patient. You were thoughtful and kind. You always listened and would respond carefully and wisely. You were always learning, always reading, always asking questions, always passionate to discover more. It made you a wonderful writer, poet, and a thorough student. It made you a marvelous husband and father. If I inherited even half of your qualities, I would consider myself a lucky woman. My grandmother, who this thesis is also dedicated to, was lucky to have you by her side for 62 grand

years. Grandma (Doris Eagle), I love you both so much and I promise to live in the memory of my grandpa. I will never forget to wonder, to dream, to try it anyways, to travel, to learn, and most importantly, to give it all I've got.

Lastly, I can't forget to share this part of my journey with my Oma and Opa. You have been pillars in my life. Thank you for always telling it like it is. Here's to all members of my family who have rooted for me along the way and continue to push me when I get distracted or discouraged. I love you all so much!

Acknowledgments

Even though this is in the beginning of the thesis, this part was written last because it is undeniably the most challenging part to attempt to begin to acknowledge those who made this milestone in my career possible.

First and foremost, I'd like to thank my co-advisor, Dr. Stefano Marchesi. Stefano has dealt with all of my agitating trouble-shooting (some politely have called it "learning"): the incessant inquiries, errors, re-occurring problems with data reduction, spectral analyses, etc. You name a potential problem and Stefano and I can guarantee we had it and Stefano was always able to fix it. Not only has he been hugely helpful in the learning process of the tasks discussed in this thesis, but his patience is astounding. I want to personally recognize Stefano's willingness to work with me day and night and (somehow) remain calm and patient with me. You have done great things before and during your time at Clemson and I know you will continue to be a great scientist and amazing mentor to many people and projects in Bologna, Italy and beyond. Thank you for everything you have taught me! You have enabled my success at Clemson more than you will ever know.

Secondly, I need to give a shout out to my supervisor, Dr. Marco Ajello, who invited me to start on this research project in the first place. I was open-minded to research projects within the astronomy field upon coming to Clemson but, when I learned of Marco's research focus and spoke with him many times regarding his work, I got tunnel vision for this particular topic. I am absolutely in love with the violent nature of these objects; Everyday my work amazes me. The universe is far more unforgiving, tumultuous, and chaotic than we could ever have dreamed and I am lucky enough to be able to characterize these phenomena. It almost makes me feel sorry for those who didn't chose this career path because they are missing out on all of the fun and especially, the wonder.

Marco has been supportive, kind, and patient as well. He is active in his role as supervisor, mentor, organizer, researcher – not just with me and my research project but with all of his graduate

students and within the scientific community. You are an inspiration, Marco! You juggle so much and are still dazzlingly successful.

Additionally, Marco has a way of making his research group feel like a family. We do many things together including skiing/snowboarding, camping, traveling to conferences and sightseeing, drinking, games, birthday celebrations, farewell parties, and more. He teaches us not *just* high energy astrophysics, but how to have a balanced and meaningful life, inside and outside of our research.

...And Marco, I am sorry but, after Stefano leaves, you may (*will*) be seeing more of my flaws and ability to destroy all functioning software tools. I apologize in advance.

Thirdly, I'd like to extend a big thank you to my research group members and my Clemson physics community. Andrew, Allen, Jaclyn, Dani, Bri, David, Lea, Abhishek, Aman, Ross, Samalka, Xiurui, Drs. Hartmann, Leising, Meyer, Marler, and more: You have all played a role in my success and I look up to each of you. Thank you for your camaraderie, support, laughter, curiosity, mentorship, partnership, and friendship.

And lastly, thank you to to my roommate, Lydia Winn, and partner, Noah Channell, for your support and keeping me sane. Lydia, thanks for dealing with the animals when I needed to study. Thank you for being a great friend and roommate! And Noah Channell, thank you so much for always understanding whenever I needed to cancel plans or skip out on something when my academics were calling. You have been so understanding and I will need more of that as I continue on with my Ph.D. (Sorry, but I love you!)

Ultimately, there are so many of you that deserve a mention here but, if you were not listed, I sincerely hope you know your importance in my life. Cheers to the work it took to get here and cheers to more of the blood, sweat and tears it'll take to collectively try to understand what we are, where we came from, and where we are going.

Table of Contents

List of Tables

List of Figures

Chapter 1

Introduction

Several deep observations have been performed to study the Galactic plane in the TeV energy band with facilities like the H.E.S.S., MAGIC, and VERITAS ground-based Cerenkov telescopes [8, 13, 14, 37]. These surveys led to the discovery that the Galactic plane is rich with TeV γ-ray emission from objects leftover after supernova explosions, such as pulsar wind nebulae (PWNe) and supernova remnants (SNRs) [5, 19, 33, 50].

Recently, the Pass 8 [11] event level reconstruction and analysis has enabled the *Fermi*-Large Area Telescope (LAT) to achieve comparable performances to the aforementioned facilities at energies above 50 GeV, reaching an average sensitivity in the plane of $\sim 2\%$ of the Crab flux (only slightly less sensitive than H.E.S.S. in this energy energy band, see [36]) with a localization accuracy better than $3'$ for most sources [9]. *Fermi*'s main advantage is that it has surveyed the *entire* sky, and hence the Galactic plane, with uniform sensitivity and coverage whereas other telescopes are limited to detection from ground-based locations and much smaller fields of views (e.g. H.E.S.S., VERITAS, and MAGIC are all ground-based) and are restricted from viewing the entire Galactic plane with uniform sensitivity. As a result, the *Fermi*-LAT [4, 11] has detected several new Galactic sources, some of which display very hard spectra above 50 GeV, which is a sign of efficient particle acceleration and (or) effective particle and energy dissipation processes. Understanding the properties of the very high energy (VHE) Galactic source population is crucial in order to identify the locations and mechanisms for Galactic cosmic ray acceleration.

One breakthrough that Pass 8 has enabled has been the census of the entire sky at >50 GeV reported in the 2FHL catalog [3], which is comprised of ∼360 sources detected across the entire

sky. Of these objects, 103 are detected in the Galactic plane ($| b | < 10^{\circ}$): 38 of these have been associated with Galactic objects as their counterparts, 42 are associated with blazars, and 23 are unassociated.

While none of these 23 unassociated sources has the radio and optical properties of blazars, it might still be possible to find γ-ray blazars on the Galactic plane that are undetected above the threshold of current radio surveys. A further selection criterion to classify sources as Galactic in origin is the hardness of the γ-ray spectrum at >50 GeV, since at these energies blazars generally exhibit a soft spectrum (average photon index $\Gamma \sim 3.2$), because the energy range is above the IC peak of their spectral energy distribution (SED). This is a result of the combination of the spectral shape of the energy distribution of the accelerated particles and the absorption due to the extragalactic background light [25], which results in an exponentially cut-off photon spectrum. Only $\sim$4 % of the 2FHL blazars display a power law photon index $\Gamma < 1.8$.

Among the 23 unidentified 2FHL objects located in the Galactic plane, 12 have $\Gamma < 1.8$, and hence the number of contaminant blazars in this hard-spectrum sub-sample is expected to be < 1. This sub-sample should therefore be mostly comprised of newly detected hard-spectrum Galactic objects. In this work, we focus on one of these 12 sources, 2FHL J0826.1–4500, which is located at $\sim$1.5° southwest of the Vela pulsar, PSR J0835–4510.

Vela is among the closest SNRs to Earth, being at a distance $d \approx 290$ pc [24], and it houses a middle-aged pulsar (characteristic age $t \approx 11$ kyr[1]). Given its significant complexity, the Vela region has been widely studied in the literature. The Vela pulsar sits in the central region of the SNR shell while actively fueling a large PWN $2^{\circ} \times 3^{\circ}$ in size known as Vela-X. The structure of a composite SNR is complex and heavily depends on the density of the surrounding material it expands into.

The layers of an SNR expanding through the circumstellar medium with a density gradient are discussed in [53]. The expansion of the PWN into the SNR, and the SNR expansion into the ISM are both responsible for heating ejecta and ambient material. The ejecta can confine the PWN, and as the PWN expands into the ejecta it also drives a shock, heating the material and producing thermal emission. The outer boundary of the SNR is defined by a forward shock (FS), which is the result of the material ejected from the initial explosion sweeping up the surrounding medium. It has been established that most massive stars, $>8M_{\odot}$, often collapse and explode at a relatively early age

[1]See `http://astronomy.swin.edu.au/cosmos/p/pulsar+characteristic+age` for a definition of characteristic age of a pulsar

(as early as a few Myrs for the most massive stars), and thus they leave behind supernova remnants inside or nearby the dense molecular gas clouds where they were formed. It is not uncommon then, for these SNRs to interact with these dense gas regions as the shock expands. The morphology and spectral features of the forward shock can provide information regarding such an interaction.

In this thesis, I present a multi-wavelength analysis of 2FHL J0826.1–4500, a VHE candidate Galactic source detected by *Fermi* at energies >50 GeV and located at the Western edge of the Vela SNR. In order to characterize this source, in the next chapter we introduce the Vela complex and, in more general, SNRs and their nature.

Chapter 2

Supernova Remnants

Supernova Remnants (SNRs) are the product of a supernova explosion that generally originate from two possibilities: a massive star more than 8 solar masses collapses in on itself and generates a violent explosion categorized as core collapse (CC SNRs) or type II SNe or, alternatively, from type Ia SNe which are typically the result of a white dwarf accreting mass from its companion star until it reaches the Chandrasekhar limit of $M \sim 1.4\,\mathrm{M}_{\odot}$ where, at this point, the carbon and oxygen core of the white dwarf star fails to maintain equilibrium under the additional mass, implodes, and then rebounds in a violent release of energy and matter in the form of a shock waves.

SNRs contribute to the heating of the interstellar medium (ISM) and the initial supernova explosion creates some of the heaviest elements in the universe while the SNR left behind helps distribute these into the environment. SNRs are some of the most powerful sources of energy in galaxies and are likely sources of cosmic ray acceleration. SNRs are commonly categorized in three different groups based on their radio emission structure: shell remnants, Crab-like remnants, and composite remnants[1].

Shell-type remnants are SNRs that have a distinct boundary - the forward shock - that is the initial explosion seen plowing through space, heating up and disturbing ambient medium, shocking and ionizing material [58]. A shell structure is what is observed as the shock wave propagates radially from the progenitor star position, sweeping up hot material into a shell. The edge of the remnant,

[1] All information discussed here can be found at `https://imagine.gsfc.nasa.gov/science/objects/supernova_remnants.html`

the shell, is what we observe best because there is more hot gas along our line of sight with the SNR than is seen in the middle (called *limb brightening*).

There are composite remnants which are an SNR that contains both an SNR shell and a PWN. Emission from composite remnants can be both thermal or non-thermal in origin and can vary across the remnant. Thermally dominated SNR shells can be seen in radio via synchrotron radiation but the PWN will dominate in the X-rays with clear spectral lines, indicating hot gas emission. In PWN dominated SNRs, the PWN and shell can emit brightly in both radio and X-rays. Though, typically there is a loss in spectral lines from the central region but shell spectral lines can still be detected [58].

Crab-like remnants, named after the famous *Crab* nebula, are also known as pulsar wind nebulae or plerions, and are often associated with a shell-type remnant, though they are observed to be more compact and uniform in emission than the SNR shell. PWNe are made up of highly relativistic electrons that are pushed out from the central star. The central star often generates massive magnetic fields that the electrons intermingle with producing synchrotron radiation that is visible in the X-rays to radio waves [58].

The forward shock can provide important characteristics of the SNR like age of the SNR, the kinematics of expansion, density of surrounding region, and chemical abundances. SNR age can be estimated using the velocity measurement of the forward shock which can be done through measuring the temperature of the shocked gas using X-ray spectroscopy [56]. The faster a shock is, the earlier in the expansion we are observing, thus, the younger the SNR. We can estimate the SNR age by measuring the temperature of the shocked gas if we can safely assume the gas is *isothermal*. In this method, we can model the presence of thermal line emission using a non-equilibrium ionization model that can provide an estimate on the electron temperature ($k_B T_e$) and ionization timescale, $n_e t$ (in units of s cm^{-3}), based on the fitting of the source spectrum, where n_e is the electron density of the SNR shell and t is the time since the hot gas was shocked [56]. However, many factors play into the temperature of the shocked gas for SNRs therefore these parameters may not reflect the age of the SNR accurately. For instance, the gas could have been freshly shocked by the return of the reverse shock from the SNR shell.

Because historical SNRs have been studied for long periods of time, it is possible to get an estimate on the age by tracking the rate of expansion since discovery. This is done simply by observing how much the SNR expands over the course of a certain period of time (the rate) and

dividing the total observed SNR size by this observed rate, providing a rough estimate for the SNR expansion time. This is typically most accurate for the youngest of SNRs.

A third and popular method would be to study the kinematics of the central star. This method uses the central pulsar spin period and its rate of change:

$$\tau = \frac{P}{2\dot{P}} \tag{2.1}$$

and can be used to understand the age of the pulsar (e.g. characteristic age) and thus the estimate of the SNR age.

Once a >8 stellar-mass star explodes, ejecting material in all directions, what often lay behind in the progenitor star's place is a highly-magnetized, rapidly rotating neutron rich star. These are called pulsars named after their typically very regular, rapid-rotating, beaming pulses of light along the line of sight to Earth. During the initial explosion, the matter in the core of the star is crushed against its own gravitational potential energy and pressure so violently that the protons and electrons combine together into neutrons. An initial mass system between 8 and 20 solar masses typically end their life with this fate while stars more massive have the potential to create stellar-mass black holes.

Neutron stars are some of the densest objects known as they are made up of stellar masses condensed into the sizes of cities on Earth. Pulsars can generate relativistic pulsar winds made up of highly energetic electrons and positrons mixing and creating turbulence in the ambient medium as well as shocking it, known as the (aforementioned) pulsar wind nebulae.

Together, SNRs and PWNe, are some of the most powerful sources in the Galaxy and are the some of the only known Galactic sources that can emit at such high energy regimes. It is understood that PWNe and SNRs are capable of accelerating cosmic rays (CRs) and are routinely detected at TeV energies and X-rays. PWNe readily emit across the electromagnetic spectrum powered by relativistic electrons via synchrotron emission or thermal bremsstrahlung at low energies (i.e. radio and X-ray emission) and via inverse Compton scattering (ICS) or non-thermal bremsstrahlung at high energies (i.e. γ-rays).

Understanding the stages of evolution of these objects can help understand dissipation mechanisms [23]. There are three main phases an SNR goes through as it expands and evolves into the ISM: the free expansion (i.e. energy conserving) phase, the adiabatic phase, and the snow-

plow (i.e. momentum-conserving) phase. The free expansion phase begins when the progenitor star explodes, ejecting mass and energy into its surroundings. The shock wave is the initial blast wave expanding freely as it moves radially outward from the center. This phase happens roughly at constant temperature and at constant velocity, thus energy is conserved during this phase, and this occurs for several thousand years [28]. The second phase is where the change in entropy for the SNR and its surroundings is equal to zero. The SNR shock wave quasistatically decelerates and cools. This phase is unstable for the SNR shell, introducing Rayleigh-Taylor instabilities, allowing for the shock wave ejecta to mix with swept up material from the ISM that was shocked and heated by the shock wave itself. This is known to increase the magnetic field within the SNR shell. The adiabatic phase can last for up to 20,000 years. The last phase, known as the snow-plow phase, radiative phase, or momentum-conserving phase, dominates as the blast wave continues to slow down, losing energy and velocity via radiation causing it to cool. This occurs around $T \sim 10^6\,\mathrm{K}$. At this temperature, recombination rates increase as electrons combine with heavier elements like oxygen, silicon, and nitrogen which lets the shock front radiate more efficiently and cool further. As this process ensues, it causes the SNR shell to actually decrease in size and increase in density and overtime more and more abundances of heavier atoms appear (and thus more cooling efficiency), hence the name "snow-plow" phase: As cooling takes over, it will happen more and more rapidly [23, 28].

At the end stages of the snow-plow phase, the SNR shell thins as its energy is radiated away mostly in visible light. A dense shell of cooler gas is now what encompasses a hot central plasma and will move only by the momentum previously provided by the supernova explosion. Eventually, the forward shock slows down enough to have reached equilibrium with the environment and the SNR will fade into the ambient material and become part of the ISM.

2.1 The Vela Supernova Remnant

The Vela SNR is the closest composite supernova remnant to Earth and is thought to have been created from a SN explosion about 10,000 years ago. At only 1,000 ly ($\sim 290\,\mathrm{pc}$) from Earth, it serves as a laboratory for studying the energetics and emission mechanisms powering SNRs. The composite SNR houses a middle-aged pulsar (characteristic age $t \approx 11\,\mathrm{kyr}$) and the pulsar fuels an active PWN, known as Vela-X, all within the 8°-diameter SNR shell. Given its significant complexity

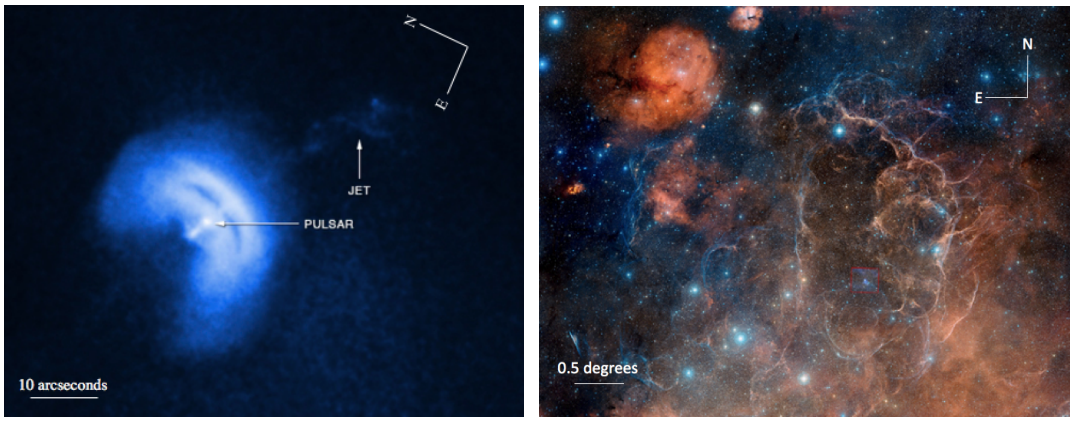

Figure 2.1: *Left*: *Chandra* 2010 image of the Vela pulsar and the small $\sim 40'$ toroidal arcs of X-ray emission. As the Vela pulsar rotates (11 rotations per second) it funnels a relativistic jet of charged particles racing from the pulsar's rotational axis. The jet imaged here is $\sim$0.7 ly in length and was discovered to be precessing. *Right*: Optical image from the Anglo-Australian Observatory's UK Schmidt telescope revealing the large apparent size of the entire Vela SNR seen to be a whopping 8° in diameter (best seen with ROSAT see figure 5.1 in section 5). The red square denotes the pulsar position.

and proximity to Earth, the Vela region has been widely studied in literature.[2]

The pulsar sits in the central region of the SNR shell while actively fueling Vela-X that is $2^\circ \times 3^\circ$ in size. The pulsar and PWN are displaced from the center of the SNR due to a combination of the pulsar's proper motion kicking it out of its birthplace (where the progenitor star collapsed), and due to the inhomogeneities in the ambient medium the SNR expands into. When an SNR expands with its forward shock into the ISM, a reverse shock is generated within from the interaction of the shock and the ISM that sweeps back across the SNR itself, crushing the PWN on its way back. The reverse shock speed depends on the density of the region the forward shock is expanding into. For example, the Vela SNR is thought to be expanding into a medium that is denser in the northern region than in the south, sending the reverse shock back *sooner* in the northern region than in the southern region, giving the PWN a displaced southern appearance from the center. This is consistent with density measurements of $n = 1 - 2\,\mathrm{cm}^{-3}$ in the north and $n \approx 0.1\,\mathrm{cm}^{-3}$ in the south [55].

Studying the particular scenario unfolding directly to the west of the Vela SNR, two facilities were used in conjunction in order to probe this peculiar unidentified VHE source. The facilities are discussed in the next chapter.

[2]Images in this section are adapted from `http://chandra.si.edu/photo/2013/vela/`

Chapter 3

Facilities

3.1 The *Fermi*-LAT

The Large Area Telescope (LAT) is the primary instrument aboard the *Fermi* Gamma-ray Space Telescope with the mission to survey the sky from energy ranges as low as 20 MeV and as high as 2 TeV with the latest Pass 8 event level analysis reconstruction [9, 10, 11][1]. The LAT was constructed by an international group of space agencies, academic institutes and universities, in France, Italy, Sweden, United States, and Japan. The LAT's original mission when it launched by NASA in June of 2008, was to determine the nature of high-energy sources such as blazars, pulsars, gamma-ray bursts (GRBs) and more that contribute to the high-energy universe. Since then, the *Fermi*-LAT has made hundreds of new discoveries of high-energy sources reported in various catalogs since its operation began[2].

The design of the LAT ultimately has seven major goals including permitting rapid notification of γ-ray bursts (GRBs) and transients and facilitating the monitoring of these variable sources, yielding a large catalog (up to several thousand high-energy sources discovered during an all-sky survey), measuring spectra from 20 MeV to more than 50 GeV for several hundred sources, optimizing uncertainties for point sources to just 0.3-2 arcminutes, mapping and obtaining the spectra of extended sources (e.g. SNRs, MCs, nearby galaxies, etc.), measuring the diffuse isotropic γ-ray background up to 2 TeV, and finally, exploring the discovery space for dark matter (i.e. tracers of

[1] All figures in this section have been adapted from [10]

[2] See: `https://heasarc.gsfc.nasa.gov/docs/cgro/db-perl/W3Browse/w3table.pl?MissionHelp=fermi` for a complete list of the *Fermi*-LAT catalogs.

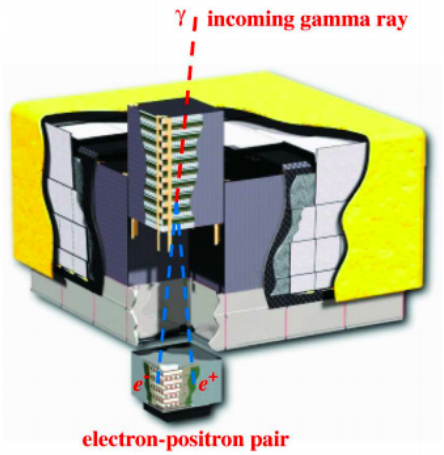

Figure 3.1: The basic design of the *Fermi*-LAT.

DM annihilation). The goal of this section is to familiarize ourselves with the basics of the instrument in order to better understand how the data for the reported source, 2FHL J0826.1-4500, was obtained. This includes the LAT general instrument design and performance of the most recent software update, Pass 8.

3.1.1 Instrumental Design

The LAT measures the directions, energies, and arrival times of incident γ-rays over a large FoV while simultaneously rejecting background from cosmic rays. The LAT is a pair-conversion telescope with a precision converter-tracker and a calorimeter, a segmented anti-coincidence detector, and a programmable trigger and data acquisition system. Pair conversion detection is an efficient method to detect γ-rays in the high-energy regime because it is known that high-energy γ-rays are not easily reflected or refracted and only interact with matter by the conversion of one γ-ray photon into an electron and positron pair.

The LAT is composed of 16 identical towers disposed in a 4×4 array. Each tower has a precision tracker and a calorimeter. The towers are aligned on a low-mass Aluminum grid design and the segmented anti-coincidence detector covers the 16 towers. Each module in the precision tracker is accompanied by a series of 18 vertical tracking planes including two layers, denoted x and y, of single-side silicon strip detectors (SSDs) and a high-Z converter material (tungsten) per tray. The SSDs act as small position-sensitive detectors to record the passage of charged particles and measuring the paths of particles that result from pair conversion. This is done by the e^-e^+ pair

hitting the SSDs causing ionization and thus creating a small electrical pulse that is then detected by the SSD. In this way, the tracker can tell which part of the sky the incident γ-ray came from.

Once the particles have left the tracker they enter the calorimeter. The calorimeter has the same design of a 4×4 array of 16 modules but each have 96 Cesium iodide scintillator crystals instead of SSDs. With this design, the longitudinal and transverse information about the deposited energy are both known and this is what enables the high-energy reach of the LAT. The calorimeter's depth and segmentation also significantly contribute to the background rejection. A larger field of view of 2.4 str ($\sim$20% of sky) is possible due to the aspect ratio, height/width (=0.4), of the tracker which also ensures that the majority of all pair-conversion showers initiated in the tracker will pass into the calorimeter for energy measurement.

The segmented anti-coincidence detector (ACD) covers the tracker array in order to provide protection from contamination of cosmic rays. For this reason it is designed to have a high detection efficiency of charged particles. It is reported in [10] that the efficiency of the ACD reaches 0.9997 for a single charged particle detection.

The programmable trigger and data acquisition system utilizes prompt signals available from the precision tracker, calorimeter, and anti-coincidence detector subsystems to form a trigger. Once an event is triggered, the data acquisition system (DAQ) initiates the read out of the 3 subsystems and uses on-board event processing to reduce the rate of events transmitted to the ground to a rate compatible with the 1 Mbps bandwidth that is available to the LAT. The maximized number of events triggered by γ-rays are transmitted to the ground while the on-board processing rejects events triggered by cosmic background particles. Heat pipes are used throughout the grid to keep the unit from over-heating.

In summary, the LAT is designed to provide good angular resolution for source localization and broadband as well as a high sensitivity over a large field of view to monitor variability and detecting transients. A sensitive calorimeter is installed over an extended energy band (50 GeV-2 TeV) to study spectral breaks and energy cut-offs. Reliable calibration and stability offers long term flux measurement. The normal to the front of the instrument (z axis) is on alternate orbits (i.e. "scanning" mode) of $\pm 35^\circ$ from the zenith, rocking northward in one orbit and south the next, in order to measure the entire sky in almost uniform sensitivity after about 2 orbits (which takes the *Fermi*-LAT about 3 hours at 565 km and a 25.5° inclination).

3.1.2 Pass 8

The event-level analysis is the name given to the process which involves event reconstruction, the measurement of the event energy and direction, and the final event classification. Before the Pass 8 event-level analysis, the LAT framework was largely developed with Monte-Carlo simulations and the initial event-level analysis upon launch was Pass 6 to which Pass 7 followed with the first improvements to the analysis after launch. The main effort for the Pass 8 event-level analysis was to target the loss of effective area of the LAT due to residual signals coming from out-of-time cosmic ray events [11]. In the Pass 8, the main areas for improvement include the Monte Carlo simulation of the detector, event reconstruction, and background rejection.

The reconstruction improvements were made to the tracker, calorimeter, and ACD. The tracker reconstruction code was modified to fix four areas of operation. The problematic areas begin with the track-following algorithm needing an initial direction to start the track following in order to understand the path the e^-e^+ pair took to trace where the photon actually underwent conversion. The second problem arises in the track model that includes multiple Coulomb scattering but this requires an estimate of the track energy which is measured from the calorimeter. These two problems make the tracker dependent on the accuracy of the calorimeter reconstruction which means the residual signals coming from out-of-time cosmic rays (i.e. ghost signals) that confuse the calorimeter also becomes a problem with the tracker. Third, pair conversion rarely has a clean path. In reality, a single pair conversion will create multiple detections as the electromagnetic shower develops. The last area that the tracker reconstruction in Pass 8 aims to rectify is that when off-axis photons deposit large energies into the calorimeter this can cause particles to move upwards in the calorimeter and start randomly hitting strips which can wash out some of the real signal. Together these problems cause a loss of events that fail to reconstruct at all, the mixing of events from the center of the point spread function (PSF) to the outer edges due to the poorly reconstructed tracks, and ultimately confusing good γ-ray events as background.

Pass 8 addresses these issues by using a global approach called tree-based tracking. Essentially, when a shower of particles begins, the tree-based tracking looks to the the conversion in the tracker to try to model the process of the shower as the electron and positron interact with the tracker and radiate energy. Once the trajectories of the particles are known, they are fit using the Kalman Filter technique and this will account for multiple scattering. This part of the Pass 8

reconstruction will reduce the fraction of mis-tracked events and boost the high-energy acceptance by 15-20% and also provides improvement for the off-axis effective area of the instrument [11].

The Pass 8 reconstruction for the calorimeter introduces a clustering stage which helps the calorimeter to identify ghost signals and recover any loss in the effective area. This technique is borrowed from graph theory and has proved to be optimal with Pass 8 up to 1 TeV (above 1 TeV, saturation becomes an issue).

The first major improvement of the ACD is the incorporation of the calorimeter's information when configuring incident particle direction with the deposited energy in the ACD. Now, directional information measured from the calorimeter clusters is propagated to the ACD, accompanied by the paths measured by the tracker. This aids in identifying background information at high energies or large incident angles as this is more susceptible to tracking errors. Secondly, when associating tracks and clusters with energy depositions in the ACD, the ACD utilizes event-by-event directional uncertainties and this new approach will significantly enhance information about background rejection. At low energies, the use of trigger information in background rejection removes the ghost signals from the ACD and substantially increases effective area. This is done by taking advantage of the fast ACD signals from the LAT trigger.

The Pass 8 event level reconstruction can increase acceptance (relative to Pass 7) by $\sim 25\%$ at high energies and, at energies below 300 MeV, as high as a factor of 3. The improvements of the 3 subsystems on the LAT will allow for the detection of multi-photon events whereas previously, the lack of calorimeter clustering along with background rejection almost completely washes away any meaningful signal the LAT might have with such events. Pass 8 has extended the energy reach of the LAT both below 100 MeV and above 1 TeV[3].

3.2 XMM-*Newton*

The X-ray Multi-Mirror-Newton (XMM-*Newton*) telescope was launched on December 10, 1999 by the European Space Agency (ESA). The XMM-*Newton* telescope has paved the way for X-ray astronomy's development since most extraterrestrial X-rays get blocked by the Earth's atmosphere, thus we can gather X-ray information on nearly a million sources from an orbiting X-ray telescope satellite. Furthermore, the design of the XMM-*Newton* telescope offers the largest effective

[3] All information described here can be found in more detail in [10] and [11].

area of all previous X-ray telescopes in the 0.5-10 keV range[4]. The satellite has an eccentric orbit, reaching nearly 33% of the Moon's distance. In this way, long term observations are able to be made with little to no interruptions. The XMM-*Newton* satellite consists of five X-ray imaging cameras and spectrographs, and an optical monitoring telescope.

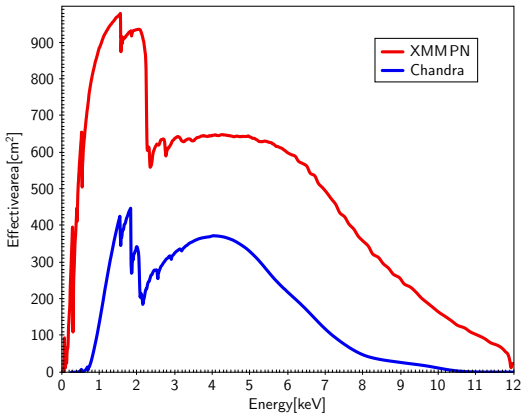

Figure 3.2: Comparing the effective area of XMM-*Newton* and the *Chandra* X-ray telescopes from 0.5-12 keV. The spectral response for the most sensitive CCD on board the XMM-*Newton* telescope has unprecedented coverage compared to *Chandra*.

There exists separate main sections on the satellite including the body that is roughly 7 meters in length, a service module that is located toward the front end that is wider than the back end and this is also where the three mirror modules and solar arrays are attached. The focal plane structure, housing the X-ray cameras and detectors, is located at the back end. X-rays are notoriously difficult to focus because they are high-energy yet interact readily with matter. Thus, a mirror design is preferred with a surface made of a material that cannot readily absorb X-rays and can enable incident X-rays to bounce off the surface at a shallow angle ($\sim 30'$). This technique can efficiently reflect the incident X-rays to a common focal point. The optimum shape for the mirror is found to be barrel shaped, angled along their length to focus X-rays onto the detectors (see figure 3.4).

The three mirror modules are made up of 58 wafer-thin nickel mirrors, gold-plated and placed on top of each other just a few millimeters apart. The total surface area of all three mirror modules is greater than $120\,m^2$ (similar in size to a tennis court). XMM-*Newton* also carries the optical monitoring telescope, a 30 cm telescope that can observe the same region of sky as the observed X-ray source and can image in optical and ultraviolet wavelengths.

[4]All information and images discussed here with XMM-*Newton* can be found at `http://sci.esa.int/xmm-newton/`

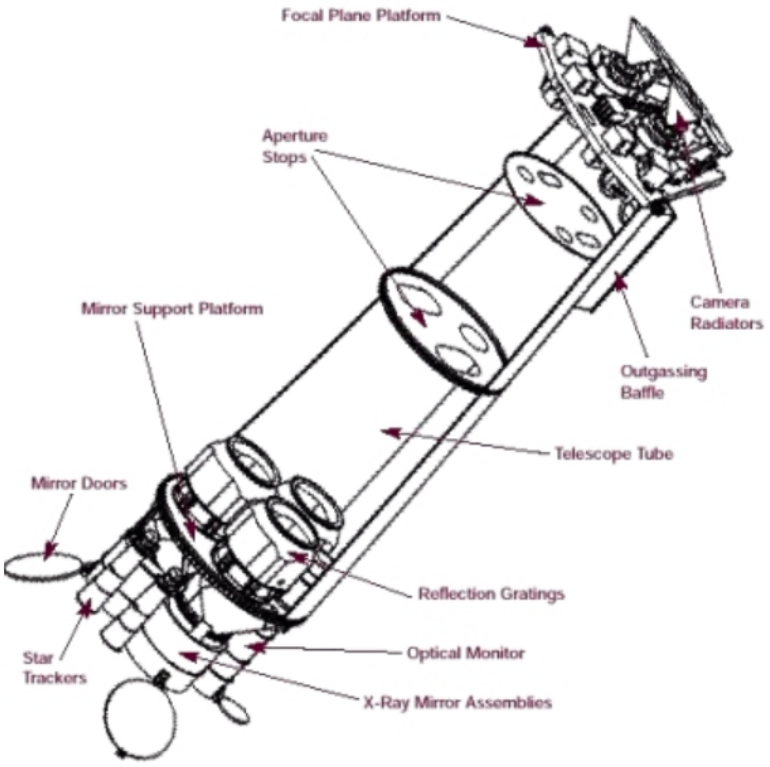

Figure 3.3: The schematic design of the XMM-*Newton* telescope. The narrower end is the back end where the three EPIC CCDs (MOS1, MOS2, and PN) sit. The wider end is where the 58 wafer-thin nickel mirror modules sit, awaiting for incident X-rays to enter the modules, reflecting and focusing efficiently onto the CCDs. The two reflection grating spectrographs lie just behind the mirror modules.

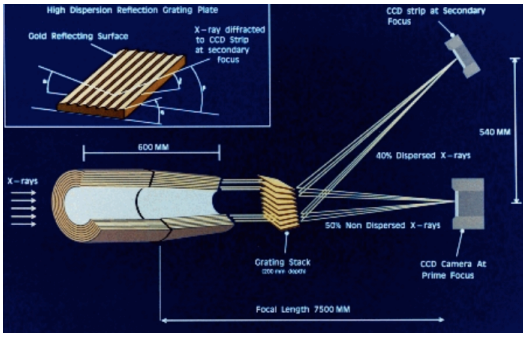

Figure 3.4: A nice schematic showing the design of the three mirror modules. MOS1 and MOS2 CCDs each have the spectrograph illustrated here.

At the focus of each of the three mirror modules are the European Photon Imaging Camera (EPIC) charged coupled devices (CCDs) comprised of silicon chips that can detect very weak X-ray signals and are capable of detecting rapid variability in intensity (as fast as 1 ms). The three EPIC cameras, MOS1, MOS2, and PN, provide imaging and spectroscopy over the field of view (about 30 arcminutes) from 0.15-15 keV. In addition to the EPIC cameras, an EPIC Radiation Monitor (ERM) is on board XMM-*Newton* to measure radiative belts and solar activity in order to supply particle environment information for proper operation of the EPIC cameras. MOS1 and MOS2 are made of metal oxide semi-conductor (MOS) 600 x 600 pixel CCDs and can detect soft X-rays with good energy resolution, though the 40μm depth of silicon limits the detectors from efficiently detecting hard X-rays. The EPIC PN makes up for this limitation which has instead a 300μm silicon depth offering more sensitivity to both soft and hard X-rays. The spatial resolution for MOS1 at 1.5 keV is 6.0 arcseconds FWHM, 4.5 arcseconds FWHM for MOS2, and 6.6 arcseconds FWHM for EPIC PN.

Two of the three mirror telescopes have a grating structure called the *Reflection Grating Spectrometer* on the module itself and can reflect roughly 40% of X-rays into a secondary focus with its own CCD camera. This design allows precise measurement of the presence of various elements like oxygen and iron.

Lastly, the 2 meter long optical monitoring telescope on board XMM-*Newton* mounted next to the X-ray mirror telescopes, is sensitive to optical and UV radiation that observes the same region as the X-ray instruments providing complementary data of the source. In orbit, and with a diameter of just 30 cm, the optical monitor is as sensitive as a 4 meter ground-based optical telescope.

XMM-*Newton* is the most sensitive X-ray observatory to be launched into Earth-orbit. Its capabilities prove to be successful including (but not limited to): investigation of cosmic X-ray source spectra, performing sensitive medium-resolution spectroscopy between 350-2500 eV, broad band imaging spectroscopy in the 150 eV-15 keV range, and simultaneous sensitive coverage in the optical.

Chapter 4

Source Selection, Data Reduction Process and Spectral Analysis

4.1 Source selection and data reduction

2FHL J0826.1−4500 was first detected at >50 GeV in the 2FHL catalog and presents a particularly hard γ-ray spectrum with photon index $\Gamma_\gamma = 1.6 \pm 0.3$ and a maximum energy photon of ∼412 GeV detected by the LAT (see Figure 4.1, left panel and Table 4.1). The source is compact and shows no clear evidence of extended emission beyond the point spread function of the *Fermi*-LAT in this energy range (Figure 4.1, right panel).

To further investigate the properties of this intriguing VHE object, we were granted a 20 ks XMM-*Newton* follow-up observation (proposal ID: 0782170201, PI: M. Ajello). X-ray telescopes like XMM-*Newton* play a pivotal role in identifying Galactic γ-ray sources, as they provide arcsecond-scale angular resolution allowing the identification of the correct counterparts in the crowded Galactic region [42]. Furthermore, XMM-*Newton* also has the largest effective area in the 0.5–10 keV band among all the X-ray telescopes, therefore being the most effective instrument to detect faint, diffuse X-ray emission along the Galactic plane, like the one commonly observed in PWNe and SNRs.

We report a summary of the observation details in Table 4.1.

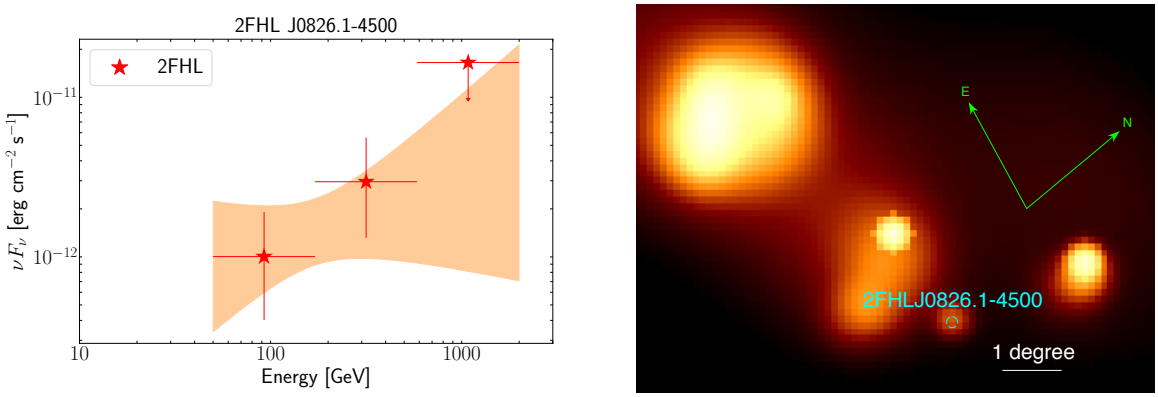

Figure 4.1: *Left*: γ-ray SED of 2FHL J0826.1−4500, using data from the 2FHL catalog [3]. *Right*: γ-ray image of the Vela complex at ≥50 GeV. 2FHL J0826.1−4500 shows no significant evidence of extended emission.

Name	R.A.	Dec.	Obs. Date	Exp.[a]	Target Type	Γ^b	Δr^c	S/N[d]
2FHL J0826.1−4500	08h 25m 56.63s	-45d 00′ 00.0″	11/23/16	18500	SNR	1.6 ±0.3	4.0	5.2

Table 4.1: Observation details of 2FHL J0826.1−4500. [a] *Exposure time in s,* [b] *Photon index at E >50 GeV,* [c] *Positional uncertainty of the γ-ray source (95% C.L.) in arc-minutes,* [d] *Signal to noise ratio of the γ-ray source (σ)*

4.2 XMM-*Newton* Data Reduction and Analysis

In Figure 4.2, left panel, we show the smoothed 0.5–2 keV image of 2FHL J0826.1−4500, as seen with the MOS2 camera mounted on XMM-*Newton*. The image was created using the CIAO [32] tool `csmooth`, using the fast fourier transforms convolution method and a Gaussian convolution kernel. The minimal signal-to-noise ratio of the signal under the kernel was set to 3. As illustrated in the X-ray image, in correspondence with the γ-ray source, we observe faint, diffuse X-ray emission with extension of roughly 15′. Furthermore, the X-ray emission is almost spatially coincident with an optical filament visible in an Hα image (see Figure 4.2, right panel). The initial analysis of the XMM-*Newton* diffuse emission reveals it to be very soft, with no significant emission detected above 2 keV.

We perform a spectral fitting in order to find the best model to characterize the observed emission. Usually, the spectral fitting of bright, point-like X-ray sources can be performed subtracting the background emission, since the signal-to-noise ratio of the source is large enough that removing a small fraction of counts from the fitted spectrum does not affect the quality of the analysis. In faint diffuse objects such as 2FHL J0826.1−4500, however, the background subtraction

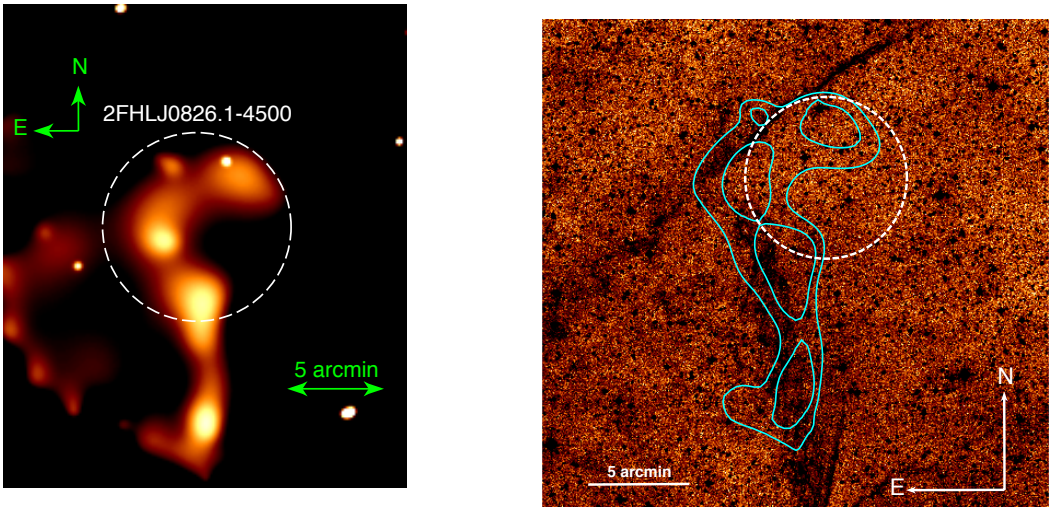

Figure 4.2: *Left*: Smoothed, MOS2 0.5–2 keV image of the region around 2FHL J0826.1−4500. The white dashed circle (r=4′) represents the 95 % confidence positional uncertainty of 2FHL J0826.1−4500. *Right*: X-ray emission contours (cyan solid line) overlaid on an Hα image of the region of 2FHL J0826.1−4500. The contours are derived from the MOS2 0.5-2 keV image shown in the left panel and correspond to 1.22×10^{-2} and 1.5×10^{-2} counts. An optical filament is seen to clearly overlap the X-ray emission. The white dashed circle marks the *Fermi*-LAT position.

approach can lead to a spectrum with not enough counts to perform a proper spectral analysis. Consequently, the background must be carefully modeled and to use the best-fit background model as an additional component in the fitting of the total, source plus background, spectrum. In this work, we follow the background modeling approach used in [40], which takes into account both the instrumental and the astrophysical background. The first is modeled as a combination of quiescent soft protons, cosmic-ray induced continuum, and fluorescence lines; the latter models both the emission from the Galactic Halo and the cosmic X-ray background[1].

The selected regions for the spectral fitting process are indicated in Figure 4.3. After selecting source and background regions a spectral fitting was then performed with the most recent update of HEASOFT software [v6.19, 26] with the corresponding calibration files for the XMM-*Newton* telescope[2] for MOS1, MOS2, and PN. The resulting spectra were fitted using XSPEC (v12.9.1).

[1] A detailed look into the background treatment methods discussed here can be found in Appendix A.
[2] Current calibration files are accessible at `https://heasarc.gsfc.nasa.gov/docs/xmm/xmmhp_caldb.html`

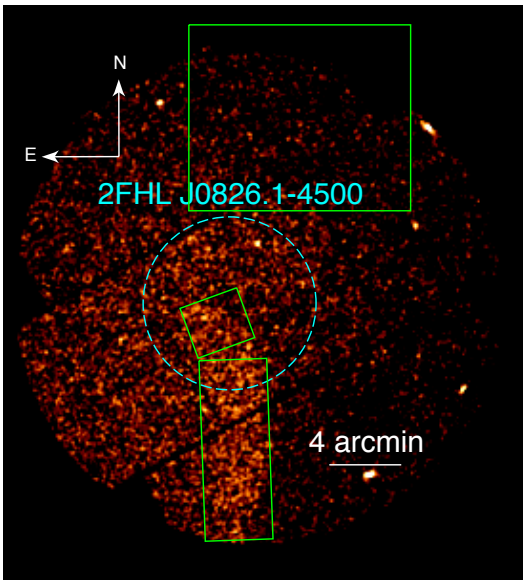

Figure 4.3: Cleaned data from MOS2 CCD with selected regions for source and background emission. The two consecutive green boxes in the lower corner are used for the source and the large green box in the upper right is used for the background.

4.3 Spectral Analysis Results

Initially, we tested two different simple spectral models: the thermal `mekal` model and a power law and both are reported in Table 4.2. The Galactic column density has been fixed to $0.026 \times 10^{22}\,\mathrm{cm}^{-2}$ [44] using `wabs` in XSPEC. The `mekal` [45, 46] model describes the emission spectrum of a hot diffuse gas, assuming as free parameters temperature and metallicity of the gas. In this work, we fix the gas metallicity to the Solar value. The `apec` model is very similar to `mekal` and was also considered. With `apec` we find a result in good agreement with `mekal` ($\mathrm{kT}=0.75^{+0.16}_{-0.20}\,\mathrm{keV}$) although with slightly worse best-fit statistics (ΔC-stat=9.7).

The power law model is commonly used to fit non-thermal spectra and has two free parameters: the photon index and the normalization. More complex power law models, such as `srcut`, `cutoffpl` and `bknpower` are typically found to best characterize synchrotron emission from a non-thermal distribution of electrons, however, due to the intrinsic faintness of our source, we decide to use the simplest of these models, a pure power law, to minimize the number of free parameters in the fit.

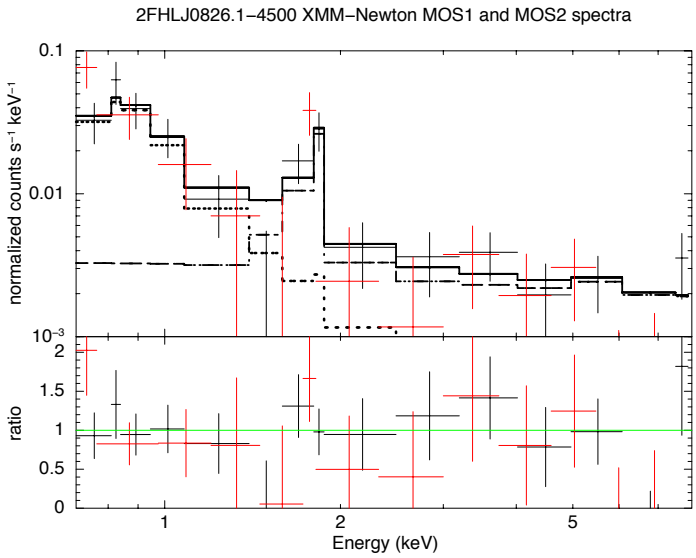

Figure 4.4: *Top*: XMM-*Newton* MOS1 (black) and MOS2 (red) data of 2FHL J0826.1−4500 and the best-fit model obtained using `mekal`. The best-fit model (solid black line), the instrumental background (dashed black line) and the combination of source and astrophysical background (dotted black line) are plotted. PN data was removed for clarity.

Spectral Model	χ^2	C-Stat	d.o.f.[a]	Reduced χ^2	kT(keV)	Photon Index
mekal	458.54	454.63	449	1.02	$0.60^{+0.11}_{-0.60}$	-
power law	472.60	470.60	451	1.05	-	$4.9^{+1.8}_{-1.2}$

Table 4.2: Summary of the best-fit parameters and the associated statistics for both spectral models used in our analysis. Because of the low quality of data, the kT value only generates an upper limit of 0.72 keV. [a] *degrees of freedom*

As shown in Table 4.2, a thermal emission scenario (Cstat/d.o.f.=454.63/449) is statistically preferred to a non-thermal one (Cstat/d.o.f.=470.60/451). The best-fit temperature is $kT = 0.60^{+0.11}_{-0.60}$ keV with an upper limit of $kT < 0.72$ keV. We show the best fit model, as well as our MOS1 and MOS2 data, in Figure 4.4. PN data has been removed for clarity. The observed 0.5–2 keV source flux, without taking into account the different background contributions, is F_X <1.9×10^{-13} erg s^{-1} cm^{-2}.

Chapter 5

Multi-wavelength Information

5.1 Soft X-rays

The Vela SNR is one of the brightest, largest soft (0.5-2 keV) X-ray sources. The ROSAT X-ray telescope [57] has mapped the Vela region in the 0.5–2.4 keV band, showing extended emission over a $\sim 8^\circ$ region that encompasses the Vela pulsar and roughly outlines the SNR shell. 2FHL J0826.1−4500 lies just on an inner boundary of X-ray emission that delineates the SNR shell where, to the west, a cavity of little X-ray emission is present (Figure 5.1). Lu & Aschenbach [41] performed a spectral analysis on 3 distinct regions of the SNR and found that the X-ray emission is best fit by a thermal emission model with two Raymond-Smith plasma components with different temperatures. The best fit temperatures are 0.12, 0.17, and 0.18 keV for T_1 and 0.76, 1.06, and 0.82 keV for T_2 in one bright region in the north and two fainter regions in the north-east and south, respectively. These results are in good agreement with those obtained by our XMM-*Newton* observation and reported in the previous section.

5.2 γ-rays

At $\geq$50 GeV, 2FHL J0826.1−4500 is a relatively faint source detected by the *Fermi*-LAT with a test statistics of $\sim$27 (corresponding to $\sim 4.5\,\sigma$) and only $\sim$5 photons [3]. In the 2FHL catalog, no evidence of extended emission at >50 GeV is reported for 2FHL J0826.1−4500, although the significance of this result is limited by the small number of counts detected by the LAT.

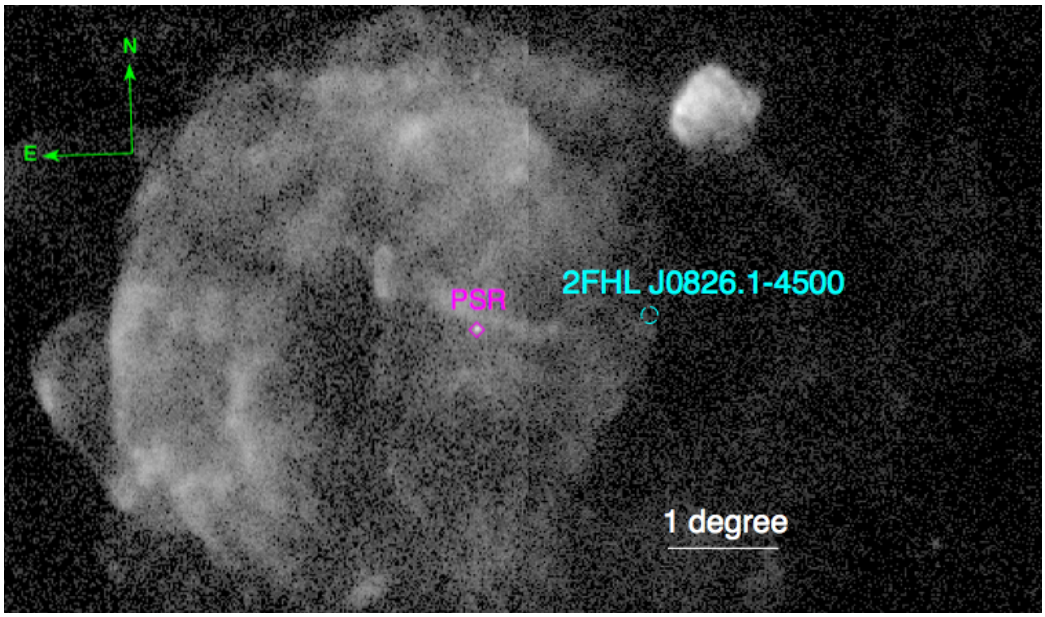

Figure 5.1: 0.5–2.4 keV ROSAT image of the Vela SNR. The cyan circle labels the γ-ray location of 2FHL J0826.1−4500 (with uncertainty of r=4′ at 95 % confidence), while the magenta diamond outlines the position of the Vela pulsar. 2FHL J0826.1−4500 lies on the western edge of a prominent X-ray shell, just before a large cavity. The bright source in the top right corner is Puppis A.

H.E.S.S. [2] found TeV emission up to 10 pc (∼1.2° from pulsar position) from the pulsar on the opposite side of the SNR with respect to 2FHL J0826.1−4500. At 1 TeV, the angular resolution for H.E.S.S. is ∼6′. The shock is approximately 15′ in length in the X-rays and it is observed by LAT up to ∼400 GeV (see Figure 4.1, left panel), so it is intriguing that H.E.S.S. did not detect any significant emission in the TeV regime at the position of 2FHL J0826.1−4500. The lack of TeV detection implies either that the spectrum of the source does not extend beyond 1 TeV or that the source is variable. It is unlikely the detection of source variability in this case will be possible with the *Fermi*-LAT because of the low photon counts of 2FHL J0826.1-4500. The recently published H.E.S.S. Galactic Plane Survey [36] allows us to derive a 5 σ upper limit on the emission of 2FHL J0826.1−4500 (assuming it is a point-like source) at >1 TeV of $F_{TeV} \approx 2.2\times10^{-13}$ erg s^{-1} cm^{-2}.

5.3 Radio

The Vela region is rich with radio emission predominantly coming from the Vela-X PWN with lower surface brightness emission roughly outlining the SNR X-ray shell. The Vela radio

Figure 5.2: *Left*: 2.4GHz radio emission map from [29][1] with location of 2FHL J0826.1−4500 seen in a cavity with no radio emission detected just below the Southwestern corner of the PWN, Vela-X. *Right*: 2.4GHz radio map zoomed to show Southwestern edge of the PWN, with the cavity 2FHL J0826.1−4500 is located in is readily seen.

emission at 2.4 GHz was investigated in [29]. When we positionally match their data with our XMM-*Newton* image we find that the X-ray emission lies on the outskirts of the diffuse radio emission. As can be seen in Figure 5.2, 2FHL J0826.1−4500 lies in a region lacking radio emission[1]. This evidence is confirmed throughout different radio observations at different frequencies. For example, observations of the ^{12}CO emission at 115 GHz revealed the same behavior of the Vela region [48].

The apparent lack of radio emission from the SNR at the position of source 2FHL J0826.1−45.00 and further west could be related to the forward shock having broken out into a lower density ISM region. This is also consistent with observations of the pulsar position and proper motion, since the pulsar is known to be in the northern part of the radio emission of the PWN. The offset is likely caused by the expansion of the SNR into the ISM and how this interacts with the PWN. It is likely that a non-uniform density in the ambient ISM is the cause of the asymmetric appearance [15, 55], and is responsible for an early return of the reverse shock of the SNR from the direction where the shock front encounters a denser medium (i.e., in this case, the structure in the Northern edge, see [55]). The atomic hydrogen density for the Northern edge of the SNR, n=1–2 cm^{-3}, is indeed greater than the one estimated for the Southern edge, $n \sim 0.1$ cm^{-3}, supporting the scenario just described [2, 27, 31].

21cm HI clouds were mapped in the Vela region reporting negative radial velocities (-21 km s^{-1} to -9 km s^{-1}) [27]. Later, Lu & Aschenbach [41] connected the high N_H column densities in the Southern region with the HI clouds observed at 21 cm, concluding that these clouds must be moving

[1]The radio maps reported in [29] are available at `http://www.atnf.csiro.au/research/surveys/2.4Gh_Southern/data.html`

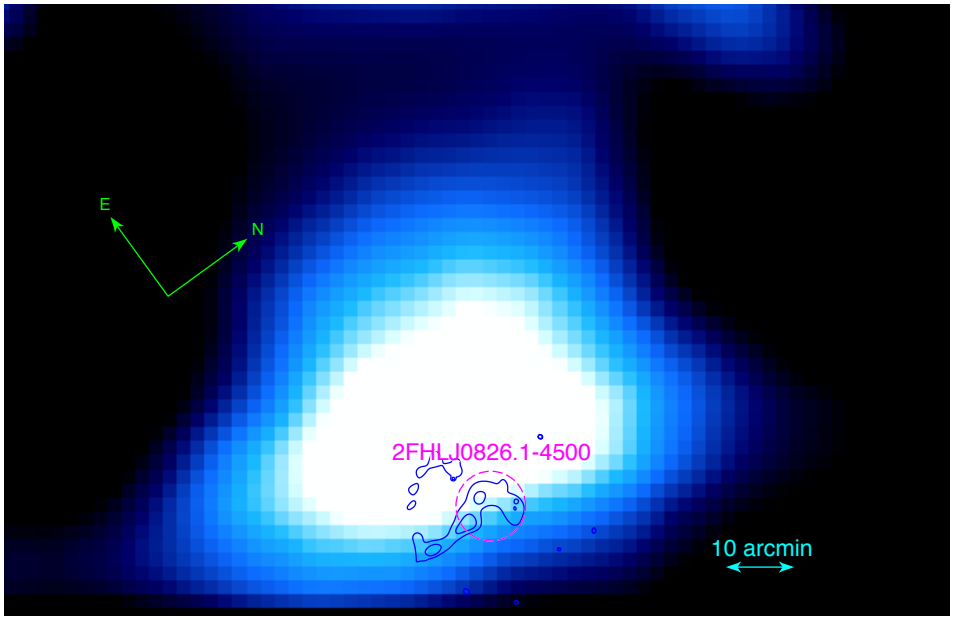

Figure 5.3: HI 21cm radio map integrated between 29.7 and 35.3 km s^{-1} indicating the location of 2FHL J0826.1−4500 with respect to the HI cloud with blue contours for reference of shock structure and location [see 27, for a review].

towards the observer and are likely being accelerated by the SNR shock wave. In [27] HI presence is interpreted as a bubble that the Vela SNR is expanding into, with a higher interaction in the North and East directions between the HI clouds and forward shock. Lu & Aschenbach [41] have speculated that the interaction is weaker with HI in the South and West directions, allowing the shock wave to keep expanding inside the bubble. This may support the idea that, at the position of 2FHL J0826.1−4500, the ROSAT X-ray boundary may be confined by the interaction with a small HI cloud. The authors in [41] also suggest that the high N_H measured implies that a region of cold interstellar gas lies behind the Southern boundary of the SNR, and that it is likely for the HI clouds to be in front of the remnant in the West, which may explain the apparent cavity that exists West of the XMM-*Newton* X-ray source.

Furthermore, a small HI cloud has been identified in [27], widely overlapping with the Hα optical filament associated with the observed XMM-*Newton* emission (see Figure 5.3). The morphology of the filament correlates well with the location and size of the HI cloud in this region, suggesting that we may be observing a shock-cloud interaction, with the shock being visible in the

the optical band and in X-rays. Notably, optical emission in SNRs is usually associated to bright X-ray boundary regions, which is indeed what is observed on the ROSAT map. This may suggest a density enhancement in the Western region of the Vela SNR, providing further evidence for a forward shock scenario.

In conclusion, the combined γ-ray, X-ray, optical and radio information depicts a scenario of interaction between a forward shock, linked to the SNR, and a HI cloud. The following section will discuss this scenario and its implications.

Chapter 6

Discussion

6.1 Shock-Cloud Interactions

Examining the X-ray and γ-ray signatures of SNR interactions with molecular clouds in [54] suggests several ways to confirm if a shock-cloud interaction is indeed occurring. Most SNRs are located within high density molecular cloud regions making shock-cloud interactions a likely occurrence with SNRs as they expand into the ISM. Morphology such as arcs, curvature, and asymmetric appearance of the SNR provide suggestive clues of an interaction with surrounding medium especially if a correlation with the shape of a nearby cloud can be established [54]. The shape of 2FHL J0826.1−4500 has a compelling overlap with the shape of the HI cloud as can be seen in Figure 5.3.

Multi-wavelength studies like the one here are another ideal way to confirm if a shock-cloud interaction is in fact happening. CO emission presence, for instance, is an efficient tool to map the distributions and movements of dense clouds, and is commonly used to confirm the physical interaction of a SNR with a molecular cloud [54].

Gathering evidence for radiative processes at the shock site will provide strong indicators for the speed of the shock front. Mapping the presence of OIII, NII, or SII optical line emission can be strong evidence for a radiative shock that is propagating into an inhomogeneous ISM [54]. More specifically, if OIII, NII, or SII are present the shock would be slower than the blast wave velocity as it comes into contact with a dense cloud. If the velocity of the shock is still considerably fast then the shock may be just starting to interact with dense material. Maser emission at 1720MHz would

also be direct evidence of excitation occurring at a site where a shock and cloud are interacting.

Substantial evidence is provided in [59] linking shock-cloud interactions to the presence of optical filaments that closely overlap X-ray emission in the SNR SN 1006. Analogously, the close coincidence between the Hα emission morphology and that of the X-ray emission in 2FHL J0826.1−4500 suggests that part of the SNR shock is interacting with a region of partially neutral material in this area.

6.2 Efficient Particle Acceleration

If 2FHL J0826.1−4500 is indeed a shock-cloud interaction region, this makes the shock location a likely candidate for efficient particle acceleration [54]. SNRs and PWNe are widely thought to generate the bulk of Galactic CRs due to their enormous energy and particle deposits into the ambient environment. Fresh generation of CRs is possible with a large hadronic population with VHE. With a large hadronic population, proton-proton collisions become frequent leading to pion decay that can be traced in the γ-ray emission. If the hadronic population is not dominant (i.e. largely leptons are present), it becomes more likely that CR production in the acceleration site is instead pre-existing CRs interacting with the region and being re-accelerated. This can still be evident in γ-ray emission and can be hard to distinguish between fresh acceleration or re-acceleration of CRs (see [22] for details).

Proton-proton collisions can become enhanced in high density regions such as an interaction between a SNR forward shock and an HI cloud. This would be a significant source of hadronic gamma-ray emission which makes the Vela SNR in the western boundary a possible source of freshly generated CRs into the Galaxy. Though there is no clear way to distinguish fresh CR acceleration from pre-existing CRs being re-accelerated, the shock site is a promising source for generating fresh CR acceleration.

Fast shocks typically reveal a potential for fresh CR acceleration by the γ-ray spectrum cutting off at energies greater than 20 GeV (e.g. SNR Cas A; see [7], RX J1713.7-3946; see [34], RX J0852.0-4622; see [6], [17], and [35]). For slow shocks this cut off occurs at energies of 10-20 GeV, indicating that the site is most likely re-accelerating pre-existing CR protons (e.g. 1FGL J1801.3-2322c; see [1], SNR W44; see [18] and [43], G349.7+0.2 and CTB 37A; see [21]).

Radiative shocks are believed to be efficient re-accelerators of the pre-existing CR population

that permeate the entire Galaxy through compression and tend to have slower velocities than the rest of the front shock. The 2FHL J0826.1−4500 shock site is certainly a candidate for efficient particle acceleration, however, a deeper analysis in VHE and optical is required in order to confirm this.

6.3 Modeling Spectral Energy Distribution

The multi-wavelength information available can be combined to build a picture of the broadband spectral characteristics of the region. Assuming the GeV γ-ray emission in the direction of 2FHL J0826.1−4500 is indeed the result of radiation from a relativistic particle population accelerated at a region of the Vela SNR shock, it is possible to model the broadband emission from the shock-accelerated non-thermally distributed electrons and protons and hence derive constraints on the physical parameters of the shock. The data of the region are shown in Figure 6.1, where the 843 MHz and 2.4 GHz radio upper limits are derived from [49] and [29] respectively, the X-ray upper limit is obtained from the XMM-*Newton* observations as described in chapter 4, and the TeV γ-ray upper limit is from the H.E.S.S. Galactic Plane Survey [36].

We assume the distribution of the accelerated particles in momentum to be $dN_i/dp = a_i\, p^{-\alpha_i} \exp\left(-p/p_{0\,i}\right)$. Here, subindex i represents the particle type (proton or electron), and α_i and $p_{0\,i}$ are the spectral index and the exponential cutoff momentum of the distributions. The coefficients for the particle distributions, a_p and a_e, are set using the total energy in relativistic particles and the electron to proton ratio as input parameters, together with the spectral shape of the distributions. The spectral indices of electron and proton distributions are assumed to be equal since analytic and semi-analytic models of particle acceleration at shocks suggest this is the case [52]. For the non-thermal radiation from these particle distributions we have used π^0-decay emission from [38, 47], synchrotron and inverse Compton (IC) emission from [12, and references therein], and non-thermal bremsstrahlung emission from [16]. For more details on the model for the particle distribution and their simulated emission see [22].

We use the model outlined above to establish the approximate ranges of some of the physical parameters that would result in emission that fits the *Fermi*-LAT data, as well as complying with the upper-limits at other wavelengths. The common parameters for all models considered are a relativistic electron to proton ratio of $k_{ep} = 0.01$ (determined in observations of CR abundances on

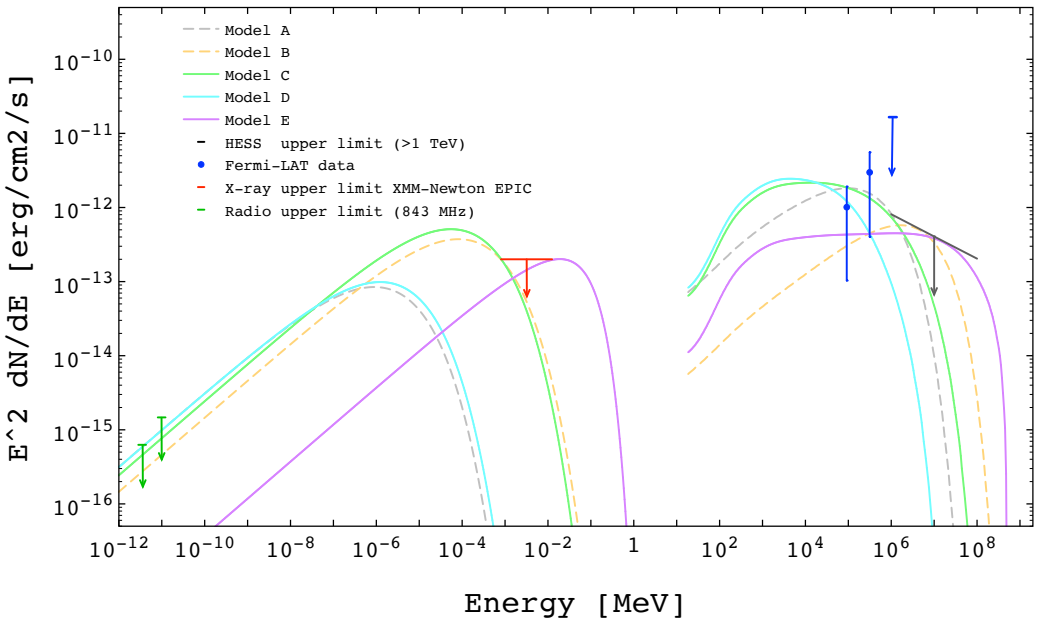

Figure 6.1: Spectral energy distribution (SED) for various scenarios constrained to upper limits of available data across the electromagnetic spectrum. Models A (gray dashed line) and B (yellow dashed line) demonstrate the resultant γ-ray spectrum of radiation from relativistic electrons. Models C (solid green), D (solid cyan), and E (solid purple) demonstrate resultant spectrum of radiation from a hadronic population.

		p_0 (TeV/c)	$B_{2,max}$ (μG)	$n_H \times E_{CR,p}$ (10^{48} erg/cm^3)	$E_{CR,e}$ (10^{44} erg)
Leptonic	*A*	5	3	–	9
	B	30	9	–	1
Hadronic	*C*	10	50	6	–
	D	1	50	6	–
	E	600	10	1	–

Table 6.1: Input Model Parameters.

Earth), and a shock compression ratio of 4. Both of these standard assumptions are discussed in more depth in [22]. It is possible that the proximity of the Vela pulsar and pulsar wind nebula, both of which are expected to be significant electron accelerators, might increase the ratio of relativistic electrons to protons present in the region of interest. A larger number of CR electrons would relax the constraints on the magnetic field placed on both leptonic and hadronic scenarios considered here. However, this effect is presumably not very significant since the γ-ray source appears to be coincident with the optical and X-ray emitting shock, and hence presumably the CRs responsible for the emission are accelerated in this same region. Additionally, we adopt a distance of $d = 0.29$ kpc (the distance of the Vela SNR, as discussed above), and fix the spectral index of the relativistic proton and electron distributions in momentum to be $\alpha_i = 4$. This last assumption is adopted given that neither the radio nor the γ-ray observations allow for a tightly constrained spectral index of the emission spectrum and hence, we default to the canonical spectral index expected from diffusive shock acceleration [see 52, and references therein]. The input parameters for each model considered are included in Table 4.2 and the resulting broadband spectral distributions are shown in Figure 6.1.

In models A and B, the *Fermi*-LAT spectrum is the result of radiation from relativistic electrons (leptonic channel), and in C, D and E, it originates from protons and heavier ions colliding with ambient hadrons and resulting in γ-ray emission from pion decay (hadronic models). Models A and B represent the highest and lowest values, respectively, for the energy CR electrons, $E_{CR,e}$, allowed by the *Fermi*-LAT data. The post-shock magnetic field, B_2, in each of these two cases, is set to the maximum value possible without the synchrotron emission exceeding the radio and X-ray limits, and the cut-off of the particle momentum distribution, p_0, is limited by the upper-limit on the TeV γ-ray emission from H.E.S.S. From these cases we estimate that if the GeV emission is the result of leptonic processes, the total CR electron energy in this region must be roughly 1–9 $\times 10^{44}$ erg, and the cut-off momentum of the particle distribution must be approximately 5–30 TeV/c. Additionally, the maximum values of the magnetic field strength seem to be between 3 and 9 μG, which are low given that one would expect values larger than 12 μG at sites of efficient particle acceleration [see 20, and references therein].

Pion decay emission is proportional to both the amount of energy in CR protons in the region, and the post-shock density [38]. Hadronic models C and D both result from the maximum values of the product $n_H \times E_{CR,p}$ allowed by the 2FHL data, and model E represents the case with the minimum $n_H \times E_{CR,p}$ possible. In models C the cut-off in proton momentum is at the highest

value allowed by the TeV upper limit, for the maximum $n_H \times E_{CR,p}$ cases. In turn, model D is the result of the minimum p_0 that still fits the GeV data. From these hadronic models we estimate the range of $n_H \times E_{CR,p}$ to be $\sim 1 - 6 \times 10^{48}$ erg/cm^3, the cut-off of the momentum distribution to be approximately $1 - 600$ TeV/c, and the maximum post-shock magnetic field strength $B_2 \sim 50$.

Chapter 7

Conclusions

The discovery and investigation of a likely shock-cloud interaction taking place on the western edge of the Vela SNR is presented. Multi-wavelength data suggests the forward shock of the SNR is interacting with a small HI cloud as a likely scenario. The data presented for 2FHL J0826.1−45.00 points towards the possibility of a site for CR acceleration. A broadband spectral fitting is reported for several particle populations that can explain the emission observed including leptonic and hadronic scenarios. In conclusion, the FS is most certainly confining protons in the region of the neutral hydrogen as the shock begins to crush the cloud, probably ionizing and heating the cloud as they interact. Because of this, it is very likely there are proton-proton collisions occuring at the shock-cloud boundary. However, we are not able to put further constraints on the particle population in this region with the SED modeling alone so a better understanding of the origin of the γ-ray emission is still needed to probe the potential for CR acceleration here.

In order to try to determine the potential for fresh CR acceleration at the site of 2FHL J0826.1–4500, we need to understand the kinematics, direction, and elemental composition of the shock. Recently we were granted one night of observing time on the Gemini-S optical and spectroscopic observatory in Chile with the 8-m telescope. Data is currently being taken in order to measure the presence of OIII and SII and data reduction should produce preliminary results in the coming months to determine the nature of acceleration of the shock-cloud interaction. See figure 7.1 for the specific details of this follow-up.

The physical conditions of 2FHL J0826.1–4500 will be valuable in better characterization of the region. This includes the understanding of the shock's kinematics and thus the energetics

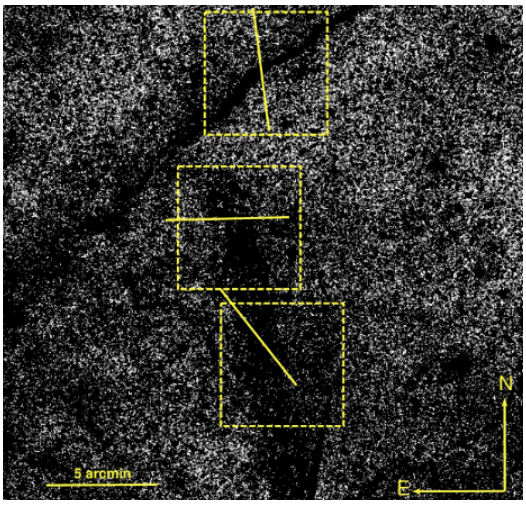

Figure 7.1: DSS2-red image of the shock which is the same as in figure 4.2, right panel, but using a different color scheme. Overlapped, are the regions where we have located the slit in each of our three pointings for the optical spectroscopy with Gemini-S. The slit locations have been chosen aiming to sample different regions of the shock while avoiding spectral contamination from stars nearby the shock. The yellow dashed boxes show the three regions where will we perform narrow-band photometry, using the [OIII] and [SII] filters.

of the environment which will provide essential clues to whether the western edge of the Vela SNR may be a site of generating fresh cosmic rays or is instead a site for re-acceleration. A paper in the future will present the findings from the Gemini-S observations followed by an interpretation of the possibility for CR production at the shock-cloud site.

Appendices

Appendix A XMM-*Newton* Data Reduction & Spectral Analysis

In this section we describe the data reduction process used to analyze and fit our observational data from XMM-*Newton* of 2FHL J0826.1–4500. In section A.1 we discuss the procedure for cleaning the event files from the telescope and in section A.2 we describe the spectral fitting method of the source and background emission.

A.1 Data Reduction

Performing data reduction on XMM-*Newton* observations requires the latest version of the SAS software tool. In this thesis SAS v17.0 is used. Additionally, the corresponding calibration files for the time of observations need to be acquired (and can be found here: `https://heasarc.gsfc.nasa.gov/docs/xmm/xmmhp_caldb.html`). The calibration files for XMM-*Newton* are regularly updated to include current information about the CCD cameras onboard the telescope. Good and bad pixels are identified as well as the efficiency of collecting X-ray photons for each pixel and these are appropriately accounted for using the corresponding calibration files for each observation. Damage and long-term use to the telescope affects the CCDs so, using the correct corresponding calibration file is imperative to an accurate data reduction.

With SAS, one will be able to perform a standard data reduction which is comprised of the following five basic steps:

1. Create calibrated event files for each CCD camera onboard (for MOS1, MOS2, and pn)

2. Effectively remove bad pixels and events out of the field of view

3. Extract a light curve at E>10 keV to inspect background emission and select a threshold value for the count rate to remove parts of the observation affected by strong noise

4. Create a new event file with new threshold value and generate a light curve in the 2-5 keV band to inspect soft proton flares

5. Add another threshold value of $\mu + 3\sigma$ (μ=count rate, σ=standard deviation) in the 2-5 keV band to generate the filtered event files for each camera.

Performing the five steps described above cleans the raw data accounting for instrumental contamination (i.e. hot pixels and proton flares from particle interactions in surrounding environment) and some astrophysical background contamination (i.e. cosmic rays). Steps after this depend

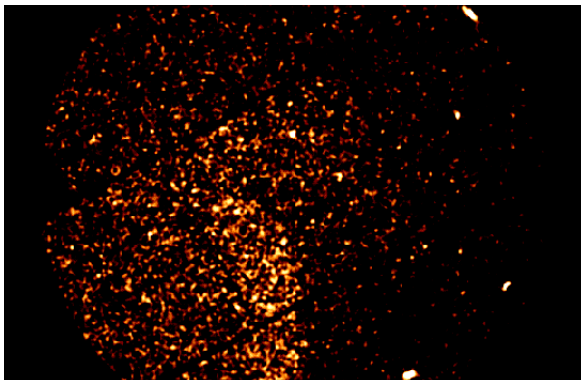

Figure 2: 0.5–10 keV XMM-*Newton* cleaned raw-data image of 2FHL J0826.1–4500. Faint X-ray emission can be seen as an arc to the lower left corner of the image. The rest is emission coming from the instrumental and astrophysical background.

on whether the source is extended or not. The cleaning procedure will remove emission that spills over from the camera's FoV as well as "bad events" (e.g. hot pixels and cosmic rays) and soft proton flares. When this is done, the final cleaned raw image of the data is complete. See figure 2 for an example of a cleaned raw-data image.

If the source is extended, the point spread function (PSF) of XMM-*Newton* needs to be calculated for each observation and this will require the creation of another file, the detector event file, and this will be used to determine the PSF in different parts of the detector and will become important when developing the auxiliary response file for the spectral fitting procedure. If the source is point like, this step is not required.

Regardless of extension, source and background regions need to be appropriately specified with the selected background regions excluding any lingering point-like sources (see section 4 and figure 4.3 for an application).

Once the regions are specified, source and background spectra can be extracted from the cleaned raw data. First, re-scale the background contribution in the source area and then generate the redistribution matrix file (RMF) to associate a proper photon energy with each CCD camera. The last step will be generating the auxiliary response file (ARF). At this point, running `grppha` assigns the spectra the proper RMF, ARF, and background files. It may be beneficial to group counts in spectral bins to reduce noise and produce a better fit though this may make the spectral fitting procedure more difficult if the signal to noise ratio is already low. Now the spectrum of the source emission is ready to be inspected and fitted.

A.2 Spectral Analysis

The spectral fitting for XMM-*Newton* data can be done with the latest version of HEASOFT. In this analysis, the most recent version used is HEASOFT v6.19 [26] and resulting spectra were fitted using XSPEC v12.9.1.

For each region, we extracted a spectrum for each CCD camera: MOS1, MOS2, and pn and fitted them individually in XSPEC. Usually, the spectral fitting of bright, point-like X-ray sources can be performed subtracting the background emission, since the signal-to-noise ratio of the source is large enough that removing a small fraction of counts from the fitted spectrum does not affect the quality of the analysis. In faint diffuse objects such as 2FHL J0826.1−4500, however, the background subtraction approach can lead to a spectrum with not enough counts to perform a proper spectral analysis. Consequently, the background must be carefully modeled and then use the best-fit background model as an additional component in the fitting of the total, source plus background, spectrum. In this work, we follow the background modeling approach used in [40], which takes into account both the instrumental and the astrophysical background. The first is modeled as a combination of quiescent soft protons, cosmic-ray induced continuum, and fluorescence lines; the latter models both the emission from the Galactic Halo and the cosmic X-ray background.

The two different approaches, modeling the background versus subtracting the background, are used to remove noise/emission not related to the source from the spectrum. Furthermore, the statistics of the two methods varies slightly. In conditions of poor statistics, as is the case for 2FHL J0826.1–4500, the Cash statistic is more suitable than using χ^2 [40]. The Cash statistic requires the number of counts in each channel to be greater than zero and background modeling does not require strong channel grouping, error propagation, or renormalization factors but, the background subtraction method does.

In the following sections we will discuss both methods for dealing with background emission for comparison.

A.3 Background Emission Treatment

Background Subtraction: As noted above, the background subtraction method is most meaningful for bright point-like sources observed with XMM-*Newton* where subtracting background emission from the spectrum does not take a significant portion of source signal with it. The regions

defined as background regions during the data reduction process will be used in XSPEC to automatically re-scale the source area and directly subtract the background spectrum from the source spectrum.

Background Modeling: Instead of subtracting the background from the overall spectrum, it may be statistically preferred to reproduce a plausible background spectrum, taking into account all possible contributors to the X-ray emission that is *not* coming from the region of interest. This is the method used in order to perform a spectral fitting of 2FHL J0826.1–4500 and is first introduced in [40]. Modeling the background accounts for the following components: the X-ray background from the Galactic halo (described in XSPEC with the thermal model *apec*[1]), the cosmic X-ray background (follows a pegged power law modeled with XSPEC component *pegpwrlw*), quiescent soft protons (follows a broken power law modeled with XSPEC component *bknpower*), the cosmic ray induced continuum (another broken power law), and finally, fluorescence emission lines that are modelled with a gaussian (in XSPEC, *gaussian*).

It is worth noting that even though we added a threshold in the data reduction to reduce noise from soft proton flares, contamination by this source is still certainly present and should be modeled when using this method. At this stage of the spectral fitting, we should have a background model and source model. The parameters of the background model are allowed to vary within 1σ errors as this has been shown to be the most accurate when modeling the background.

In conclusion, depending on the brightness of the region of interest (ROI) in the X-rays observed with XMM-*Newton* one may find one treatment for the background emission more suitable than the other and so this should be considered when performing any spectral analysis.

[1]Descriptions of XSPEC model components can be found here: `https://heasarc.gsfc.nasa.gov/xanadu/xspec/manual/Models.html`

Bibliography

[1] A. A. Abdo, M. Ackermann, M. Ajello, A. Allafort, L. Baldini, J. Ballet, G. Barbiellini, D. Bastieri, K. Bechtol, R. Bellazzini, B. Berenji, R. D. Blandford, E. D. Bloom, E. Bonamente, A. W. Borgland, A. Bouvier, T. J. Brandt, J. Bregeon, M. Brigida, P. Bruel, R. Buehler, S. Buson, G. A. Caliandro, R. A. Cameron, P. A. Caraveo, S. Carrigan, J. M. Casandjian, C. Cecchi, Ö. Çelik, A. Chekhtman, J. Chiang, S. Ciprini, R. Claus, J. Cohen-Tanugi, J. Conrad, C. D. Dermer, F. de Palma, E. d. C. e. Silva, P. S. Drell, R. Dubois, D. Dumora, C. Farnier, C. Favuzzi, S. J. Fegan, Y. Fukazawa, Y. Fukui, S. Funk, P. Fusco, F. Gargano, N. Gehrels, S. Germani, N. Giglietto, F. Giordano, T. Glanzman, G. Godfrey, I. A. Grenier, J. E. Grove, S. Guiriec, D. Hadasch, Y. Hanabata, A. K. Harding, E. Hays, D. Horan, R. E. Hughes, G. Jóhannesson, A. S. Johnson, W. N. Johnson, T. Kamae, H. Katagiri, J. Kataoka, J. Knödlseder, M. Kuss, J. Lande, L. Latronico, S.-H. Lee, M. Lemoine-Goumard, M. Llena Garde, F. Longo, F. Loparco, M. N. Lovellette, P. Lubrano, A. Makeev, M. N. Mazziotta, P. F. Michelson, W. Mitthumsiri, T. Mizuno, A. A. Moiseev, C. Monte, M. E. Monzani, A. Morselli, I. V. Moskalenko, S. Murgia, T. Nakamori, P. L. Nolan, J. P. Norris, E. Nuss, M. Ohno, T. Ohsugi, N. Omodei, E. Orlando, J. F. Ormes, M. Ozaki, J. H. Panetta, D. Parent, V. Pelassa, M. Pepe, M. Pesce-Rollins, F. Piron, T. A. Porter, S. Rainò, R. Rando, M. Razzano, A. Reimer, O. Reimer, T. Reposeur, A. Y. Rodriguez, M. Roth, H. F.-W. Sadrozinski, A. Sander, P. M. Saz Parkinson, C. Sgrò, E. J. Siskind, D. A. Smith, P. D. Smith, G. Spandre, P. Spinelli, M. S. Strickman, D. J. Suson, H. Tajima, H. Takahashi, T. Takahashi, T. Tanaka, J. B. Thayer, J. G. Thayer, D. J. Thompson, L. Tibaldo, O. Tibolla, D. F. Torres, G. Tosti, Y. Uchiyama, T. Uehara, T. L. Usher, V. Vasileiou, N. Vilchez, V. Vitale, A. P. Waite, P. Wang, B. L. Winer, K. S. Wood, H. Yamamoto, R. Yamazaki, Z. Yang, T. Ylinen, and M. Ziegler. Fermi Large Area Telescope Observations of the Supernova Remnant W28 (G6.4-0.1). *ApJ*, 718:348–356, July 2010.

[2] A. Abramowski, F. Acero, F. Aharonian, A. G. Akhperjanian, G. Anton, S. Balenderan, A. Balzer, A. Barnacka, Y. Becherini, J. Becker Tjus, K. Bernlöhr, E. Birsin, J. Biteau, A. Bochow, C. Boisson, J. Bolmont, P. Bordas, J. Brucker, F. Brun, P. Brun, T. Bulik, S. Carrigan, S. Casanova, M. Cerruti, P. M. Chadwick, A. Charbonnier, R. C. G. Chaves, A. Cheesebrough, G. Cologna, J. Conrad, C. Couturier, M. Dalton, M. K. Daniel, I. D. Davids, B. Degrange, C. Deil, P. deWilt, H. J. Dickinson, A. Djannati-Ataï, W. Domainko, L. O. '. Drury, F. Dubois, G. Dubus, K. Dutson, J. Dyks, M. Dyrda, K. Egberts, P. Eger, P. Espigat, L. Fallon, C. Farnier, S. Fegan, F. Feinstein, M. V. Fernandes, D. Fernandez, A. Fiasson, G. Fontaine, A. Förster, M. Füßling, M. Gajdus, Y. A. Gallant, T. Garrigoux, H. Gast, B. Giebels, J. F. Glicenstein, B. Glück, D. Göring, M.-H. Grondin, S. Häffner, J. D. Hague, J. Hahn, D. Hampf, J. Harris, S. Heinz, G. Heinzelmann, G. Henri, G. Hermann, A. Hillert, J. A. Hinton, W. Hofmann, P. Hofverberg, M. Holler, D. Horns, A. Jacholkowska, C. Jahn, M. Jamrozy, I. Jung, M. A. Kastendieck, K. Katarzyński, U. Katz, S. Kaufmann, B. Khélifi, D. Klochkov, W. Kluźniak, T. Kneiske, N. Komin, K. Kosack, R. Kossakowski, F. Krayzel, P. P. Krüger, H. Laffon, G. Lamanna, J.-P. Lenain, D. Lennarz, T. Lohse, A. Lopatin, C.-C. Lu, V. Marandon, A. Marcowith, J. Masbou, G. Maurin, N. Maxted, M. Mayer, T. J. L. McComb, M. C. Medina,

J. Méhault, U. Menzler, R. Moderski, M. Mohamed, E. Moulin, C. L. Naumann, M. Naumann-Godo, M. de Naurois, D. Nedbal, N. Nguyen, J. Niemiec, S. J. Nolan, S. Ohm, E. de Oña Wilhelmi, B. Opitz, M. Ostrowski, I. Oya, M. Panter, D. Parsons, M. Paz Arribas, N. W. Pekeur, G. Pelletier, J. Perez, P.-O. Petrucci, B. Peyaud, S. Pita, G. Pühlhofer, M. Punch, A. Quirrenbach, M. Raue, A. Reimer, O. Reimer, M. Renaud, R. de los Reyes, F. Rieger, J. Ripken, L. Rob, S. Rosier-Lees, G. Rowell, B. Rudak, C. B. Rulten, V. Sahakian, D. A. Sanchez, A. Santangelo, R. Schlickeiser, A. Schulz, U. Schwanke, S. Schwarzburg, S. Schwemmer, F. Sheidaei, J. L. Skilton, H. Sol, G. Spengler, Ł. Stawarz, R. Steenkamp, C. Stegmann, F. Stinzing, K. Stycz, I. Sushch, A. Szostek, J.-P. Tavernet, R. Terrier, M. Tluczykont, C. Trichard, K. Valerius, C. van Eldik, G. Vasileiadis, C. Venter, A. Viana, P. Vincent, H. J. Völk, F. Volpe, S. Vorobiov, M. Vorster, S. J. Wagner, M. Ward, R. White, A. Wierzcholska, D. Wouters, M. Zacharias, A. Zajczyk, A. A. Zdziarski, A. Zech, and H.-S. Zechlin. Probing the extent of the non-thermal emission from the Vela X region at TeV energies with H.E.S.S. *A&A*, 548:A38, December 2012.

[3] M. Ackermann, M. Ajello, W. B. Atwood, L. Baldini, J. Ballet, G. Barbiellini, D. Bastieri, J. Becerra Gonzalez, R. Bellazzini, E. Bissaldi, R. D. Blandford, E. D. Bloom, R. Bonino, E. Bottacini, T. J. Brandt, J. Bregeon, P. Bruel, R. Buehler, S. Buson, G. A. Caliandro, R. A. Cameron, R. Caputo, M. Caragiulo, P. A. Caraveo, E. Cavazzuti, C. Cecchi, E. Charles, A. Chekhtman, C. C. Cheung, J. Chiang, G. Chiaro, S. Ciprini, J. M. Cohen, J. Cohen-Tanugi, L. R. Cominsky, J. Conrad, A. Cuoco, S. Cutini, F. D'Ammando, A. de Angelis, F. de Palma, R. Desiante, M. Di Mauro, L. Di Venere, A. Domínguez, P. S. Drell, C. Favuzzi, S. J. Fegan, E. C. Ferrara, W. B. Focke, P. Fortin, A. Franckowiak, Y. Fukazawa, S. Funk, A. K. Furniss, P. Fusco, F. Gargano, D. Gasparrini, N. Giglietto, P. Giommi, F. Giordano, M. Giroletti, T. Glanzman, G. Godfrey, I. A. Grenier, M.-H. Grondin, L. Guillemot, S. Guiriec, A. K. Harding, E. Hays, J. W. Hewitt, A. B. Hill, D. Horan, G. Iafrate, D. Hartmann, T. Jogler, G. Jóhannesson, A. S. Johnson, T. Kamae, J. Kataoka, J. Knödlseder, M. Kuss, G. La Mura, S. Larsson, L. Latronico, M. Lemoine-Goumard, J. Li, L. Li, F. Longo, F. Loparco, B. Lott, M. N. Lovellette, P. Lubrano, G. M. Madejski, S. Maldera, A. Manfreda, M. Mayer, M. N. Mazziotta, P. F. Michelson, N. Mirabal, W. Mitthumsiri, T. Mizuno, A. A. Moiseev, M. E. Monzani, A. Morselli, I. V. Moskalenko, S. Murgia, E. Nuss, T. Ohsugi, N. Omodei, M. Orienti, E. Orlando, J. F. Ormes, D. Paneque, J. S. Perkins, M. Pesce-Rollins, V. Petrosian, F. Piron, G. Pivato, T. A. Porter, S. Rainò, R. Rando, M. Razzano, S. Razzaque, A. Reimer, O. Reimer, T. Reposeur, R. W. Romani, M. Sánchez-Conde, P. M. Saz Parkinson, J. Schmid, A. Schulz, C. Sgrò, E. J. Siskind, F. Spada, G. Spandre, P. Spinelli, D. J. Suson, H. Tajima, H. Takahashi, M. Takahashi, T. Takahashi, J. B. Thayer, D. J. Thompson, L. Tibaldo, D. F. Torres, G. Tosti, E. Troja, G. Vianello, K. S. Wood, M. Wood, M. Yassine, G. Zaharijas, and S. Zimmer. 2FHL: The Second Catalog of Hard Fermi-LAT Sources. *ApJS*, 222:5, January 2016.

[4] M. Ackermann, M. Ajello, L. Baldini, J. Ballet, G. Barbiellini, D. Bastieri, R. Bellazzini, E. Bissaldi, E. D. Bloom, R. Bonino, E. Bottacini, T. J. Brandt, J. Bregeon, P. Bruel, R. Buehler, R. A. Cameron, M. Caragiulo, P. A. Caraveo, D. Castro, E. Cavazzuti, C. Cecchi, E. Charles, A. Chekhtman, C. C. Cheung, G. Chiaro, S. Ciprini, J. M. Cohen, D. Costantin, F. Costanza, S. Cutini, F. D'Ammando, F. de Palma, R. Desiante, S. W. Digel, N. Di Lalla, M. Di Mauro, L. Di Venere, C. Favuzzi, S. J. Fegan, E. C. Ferrara, A. Franckowiak, Y. Fukazawa, S. Funk, P. Fusco, F. Gargano, D. Gasparrini, N. Giglietto, F. Giordano, M. Giroletti, D. Green, I. A. Grenier, M.-H. Grondin, L. Guillemot, S. Guiriec, A. K. Harding, E. Hays, J. W. Hewitt, D. Horan, X. Hou, G. Jóhannesson, T. Kamae, M. Kuss, G. La Mura, S. Larsson, M. Lemoine-Goumard, J. Li, F. Longo, F. Loparco, P. Lubrano, J. D. Magill, S. Maldera, D. Malyshev, A. Manfreda, M. N. Mazziotta, P. F. Michelson, W. Mitthumsiri, T. Mizuno, M. E. Monzani, A. Morselli, I. V. Moskalenko, M. Negro, E. Nuss, T. Ohsugi, N. Omodei, M. Orienti, E. Orlando, J. F. Ormes, V. S. Paliya, D. Paneque, J. S. Perkins, M. Persic, M. Pesce-Rollins, V. Petrosian, F. Piron, T. A. Porter, G. Principe, S. Rainò, R. Rando, M. Razzano, S. Razzaque,

A. Reimer, O. Reimer, T. Reposeur, C. Sgrò, D. Simone, E. J. Siskind, F. Spada, G. Spandre, P. Spinelli, D. J. Suson, D. Tak, J. B. Thayer, D. J. Thompson, D. F. Torres, G. Tosti, E. Troja, G. Vianello, K. S. Wood, and M. Wood. Search for Extended Sources in the Galactic Plane Using Six Years of Fermi-Large Area Telescope Pass 8 Data above 10 GeV. *ApJ*, 843:139, July 2017.

[5] F. Aharonian, A. G. Akhperjanian, A. R. Bazer-Bachi, M. Beilicke, W. Benbow, D. Berge, K. Bernlöhr, C. Boisson, O. Bolz, V. Borrel, I. Braun, F. Breitling, A. M. Brown, P. M. Chadwick, L.-M. Chounet, R. Cornils, L. Costamante, B. Degrange, H. J. Dickinson, A. Djannati-Ataï, L. O. Drury, G. Dubus, D. Emmanoulopoulos, P. Espigat, F. Feinstein, G. Fontaine, Y. Fuchs, S. Funk, Y. A. Gallant, B. Giebels, S. Gillessen, J. F. Glicenstein, P. Goret, C. Hadjichristidis, M. Hauser, G. Heinzelmann, G. Henri, G. Hermann, J. A. Hinton, W. Hofmann, M. Holleran, D. Horns, A. Jacholkowska, O. C. de Jager, B. Khélifi, N. Komin, A. Konopelko, I. J. Latham, R. Le Gallou, A. Lemière, M. Lemoine-Goumard, N. Leroy, T. Lohse, J. M. Martin, O. Martineau-Huynh, A. Marcowith, C. Masterson, T. J. L. McComb, M. de Naurois, S. J. Nolan, A. Noutsos, K. J. Orford, J. L. Osborne, M. Ouchrif, M. Panter, G. Pelletier, S. Pita, G. Pühlhofer, M. Punch, B. C. Raubenheimer, M. Raue, J. Raux, S. M. Rayner, A. Reimer, O. Reimer, J. Ripken, L. Rob, L. Rolland, G. Rowell, V. Sahakian, L. Saugé, S. Schlenker, R. Schlickeiser, C. Schuster, U. Schwanke, M. Siewert, H. Sol, D. Spangler, R. Steenkamp, C. Stegmann, J.-P. Tavernet, R. Terrier, C. G. Théoret, M. Tluczykont, G. Vasileiadis, C. Venter, P. Vincent, H. J. Völk, and S. J. Wagner. The H.E.S.S. Survey of the Inner Galaxy in Very High Energy Gamma Rays. *ApJ*, 636:777–797, January 2006.

[6] F. Aharonian, A. G. Akhperjanian, A. R. Bazer-Bachi, M. Beilicke, W. Benbow, D. Berge, K. Bernlöhr, C. Boisson, O. Bolz, V. Borrel, I. Braun, A. M. Brown, R. Bühler, I. Büsching, S. Carrigan, P. M. Chadwick, L.-M. Chounet, G. Coignet, R. Cornils, L. Costamante, B. Degrange, H. J. Dickinson, A. Djannati-Ataï, L. O. Drury, G. Dubus, K. Egberts, D. Emmanoulopoulos, P. Espigat, F. Feinstein, E. Ferrero, A. Fiasson, M. D. Filipovic, G. Fontaine, Y. Fukui, S. Funk, S. Funk, M. Füßling, Y. A. Gallant, B. Giebels, J. F. Glicenstein, P. Goret, C. Hadjichristidis, D. Hauser, M. Hauser, G. Heinzelmann, G. Henri, G. Hermann, J. A. Hinton, J. S. Hiraga, A. Hoffmann, W. Hofmann, M. Holleran, S. Hoppe, D. Horns, Y. Ishisaki, A. Jacholkowska, O. C. de Jager, E. Kendziorra, M. Kerschhaggl, B. Khélifi, N. Komin, A. Konopelko, K. Kosack, G. Lamanna, I. J. Latham, R. Le Gallou, A. Lemière, M. Lemoine-Goumard, T. Lohse, J. M. Martin, O. Martineau-Huynh, A. Marcowith, C. Masterson, G. Maurin, T. J. L. McComb, E. Moulin, Y. Moriguchi, M. de Naurois, D. Nedbal, S. J. Nolan, A. Noutsos, K. J. Orford, J. L. Osborne, M. Ouchrif, M. Panter, G. Pelletier, S. Pita, G. Pühlhofer, M. Punch, S. Ranchon, B. C. Raubenheimer, M. Raue, S. M. Rayner, A. Reimer, J. Ripken, L. Rob, L. Rolland, S. Rosier-Lees, G. Rowell, V. Sahakian, A. Santangelo, L. Saugé, S. Schlenker, R. Schlickeiser, R. Schröder, U. Schwanke, S. Schwarzburg, S. Schwemmer, A. Shalchi, H. Sol, D. Spangler, F. Spanier, R. Steenkamp, C. Stegmann, G. Superina, P. H. Tam, J.-P. Tavernet, R. Terrier, M. Tluczykont, C. van Eldik, G. Vasileiadis, C. Venter, J. P. Vialle, P. Vincent, H. J. Völk, S. J. Wagner, and M. Ward. H.E.S.S. Observations of the Supernova Remnant RX J0852.0-4622: Shell-Type Morphology and Spectrum of a Widely Extended Very High Energy Gamma-Ray Source. *ApJ*, 661:236–249, May 2007.

[7] M. L. Ahnen, S. Ansoldi, L. A. Antonelli, C. Arcaro, A. Babić, B. Banerjee, P. Bangale, U. Barres de Almeida, J. A. Barrio, J. Becerra González, W. Bednarek, E. Bernardini, A. Berti, W. Bhattacharyya, B. Biasuzzi, A. Biland, O. Blanch, S. Bonnefoy, G. Bonnoli, R. Carosi, A. Carosi, A. Chatterjee, M. Colak, P. Colin, E. Colombo, J. L. Contreras, J. Cortina, S. Covino, P. Cumani, P. Da Vela, F. Dazzi, A. De Angelis, B. De Lotto, E. de Oña Wilhelmi, F. Di Pierro, M. Doert, A. Domínguez, D. Dominis Prester, D. Dorner, M. Doro, S. Einecke, D. Eisenacher Glawion, D. Elsaesser, M. Engelkemeier, V. Fallah Ramazani, A. Fernández-Barral, D. Fi-

dalgo, M. V. Fonseca, L. Font, C. Fruck, D. Galindo, R. J. García López, M. Garczarczyk, M. Gaug, P. Giammaria, N. Godinović, D. Gora, D. Guberman, D. Hadasch, A. Hahn, T. Hassan, M. Hayashida, J. Herrera, J. Hose, D. Hrupec, T. Inada, K. Ishio, Y. Konno, H. Kubo, J. Kushida, D. Kuveždić, D. Lelas, E. Lindfors, S. Lombardi, F. Longo, M. López, C. Maggio, P. Majumdar, M. Makariev, G. Maneva, M. Manganaro, K. Mannheim, L. Maraschi, M. Mariotti, M. Martínez, D. Mazin, U. Menzel, M. Minev, R. Mirzoyan, A. Moralejo, V. Moreno, E. Moretti, V. Neustroev, A. Niedzwiecki, M. Nievas Rosillo, K. Nilsson, D. Ninci, K. Nishijima, K. Noda, L. Nogués, S. Paiano, J. Palacio, D. Paneque, R. Paoletti, J. M. Paredes, G. Pedaletti, M. Peresano, L. Perri, M. Persic, P. G. Prada Moroni, E. Prandini, I. Puljak, J. R. Garcia, I. Reichardt, W. Rhode, M. Ribó, J. Rico, C. Righi, T. Saito, K. Satalecka, S. Schroeder, T. Schweizer, S. N. Shore, J. Sitarek, I. Šnidarić, D. Sobczynska, A. Stamerra, M. Strzys, T. Surić, L. Takalo, F. Tavecchio, P. Temnikov, T. Terzić, D. Tescaro, M. Teshima, N. Torres-Albà, A. Treves, G. Vanzo, M. Vazquez Acosta, I. Vovk, J. E. Ward, M. Will, and D. Zarić. A cut-off in the TeV gamma-ray spectrum of the SNR Cassiopeia A. *MNRAS*, 472:2956–2962, December 2017.

[8] L. A. Antonelli, P. Blasi, G. Bonanno, O. Catalano, S. Covino, A. De Angelis, B. De Lotto, M. Ghigo, G. Ghisellini, G. L. Israel, A. La Barbera, G. Pareschi, M. Persic, M. Roncadelli, B. Sacco, M. Salvati, F. Tavecchio, and P. Vallania. The Next Generation of Cherenkov Telescopes. A White Paper for the Italian National Institute for Astrophysics (INAF). *ArXiv e-prints*, June 2009.

[9] W. Atwood, A. Albert, L. Baldini, M. Tinivella, J. Bregeon, M. Pesce-Rollins, C. Sgrò, P. Bruel, E. Charles, A. Drlica-Wagner, A. Franckowiak, T. Jogler, L. Rochester, T. Usher, M. Wood, J. Cohen-Tanugi, and S. Zimmer for the Fermi-LAT Collaboration. Pass 8: Toward the Full Realization of the Fermi-LAT Scientific Potential. *ArXiv e-prints*, March 2013.

[10] W. B. Atwood, A. A. Abdo, M. Ackermann, W. Althouse, B. Anderson, M. Axelsson, L. Baldini, J. Ballet, D. L. Band, G. Barbiellini, and et al. The Large Area Telescope on the Fermi Gamma-Ray Space Telescope Mission. *ApJ*, 697:1071–1102, June 2009.

[11] W. B. Atwood, L. Baldini, J. Bregeon, P. Bruel, A. Chekhtman, J. Cohen-Tanugi, A. Drlica-Wagner, J. Granot, F. Longo, N. Omodei, M. Pesce-Rollins, S. Razzaque, L. S. Rochester, C. Sgrò, M. Tinivella, T. L. Usher, and S. Zimmer. New Fermi-LAT Event Reconstruction Reveals More High-energy Gamma Rays from Gamma-Ray Bursts. *ApJ*, 774:76, September 2013.

[12] M. G. Baring, D. C. Ellison, S. P. Reynolds, I. A. Grenier, and P. Goret. *Radio to Gamma-Ray Emission from Shell-Type Supernova Remnants: Predictions from Nonlinear Shock Acceleration Models. ApJ*, 513:311–338, March 1999.

[13] K. Bernlöhr, O. Carrol, R. Cornils, S. Elfahem, P. Espigat, S. Gillessen, G. Heinzelmann, G. Hermann, W. Hofmann, D. Horns, I. Jung, R. Kankanyan, A. Katona, B. Khelifi, H. Krawczynski, M. Panter, M. Punch, S. Rayner, G. Rowell, M. Tluczykont, and R. van Staa. The optical system of the H.E.S.S. imaging atmospheric Cherenkov telescopes. Part I: layout and components of the system. *Astroparticle Physics*, 20:111–128, November 2003.

[14] C. Bigongiari. The MAGIC telescope. In *International Europhysics Conference on High Energy Physics, HEP2005*, page 20, 2005.

[15] J. M. Blondin, R. A. Chevalier, and D. M. Frierson. Pulsar Wind Nebulae in Evolved Supernova Remnants. *ApJ*, 563:806–815, December 2001.

[16] A. M. Bykov, R. A. Chevalier, D. C. Ellison, and Y. A. Uvarov. *Nonthermal Emission from a Supernova Remnant in a Molecular Cloud. ApJ*, 538:203–216, July 2000.

[17] A. M. Bykov, D. C. Ellison, A. Marcowith, and S. M. Osipov. Cosmic Ray Production in Supernovae. , 214:41, February 2018.

[18] M. Cardillo, E. Amato, and P. Blasi. Supernova remnant W44: a case of cosmic-ray reacceleration. *A&A*, 595:A58, October 2016.

[19] S. Carrigan, F. Brun, R. C. G. Chaves, C. Deil, H. Gast, V. Marandon, and for the H. E. S. S. collaboration. Charting the TeV Milky Way: H.E.S.S. Galactic plane survey maps, catalog and source populations. *ArXiv e-prints*, July 2013.

[20] D. Castro, L. A. Lopez, P. O. Slane, H. Yamaguchi, E. Ramirez-Ruiz, and E. Figueroa-Feliciano. *A Chandra View of Non-thermal Emission in the Northwestern Region of Supernova Remnant RCW 86: Particle Acceleration and Magnetic Fields. ApJ*, 779:49, December 2013.

[21] D. Castro and P. Slane. Fermi Large Area Telescope Observations of Supernova Remnants Interacting with Molecular Clouds. *ApJ*, 717:372–378, July 2010.

[22] D. Castro, P. Slane, A. Carlton, and E. Figueroa-Feliciano. *Fermi-LAT Observations of Supernova Remnants Interacting with Molecular Clouds: W41, MSH 17-39, and G337.7-0.1. ApJ*, 774:36, September 2013.

[23] R. A. Chevalier. The interaction of supernovae with the interstellar medium. , 15:175–196, 1977.

[24] R. Dodson, D. Legge, J. E. Reynolds, and P. M. McCulloch. The Vela Pulsar's Proper Motion and Parallax Derived from VLBI Observations. *ApJ*, 596:1137–1141, October 2003.

[25] A. Domínguez, J. R. Primack, D. J. Rosario, F. Prada, R. C. Gilmore, S. M. Faber, D. C. Koo, R. S. Somerville, M. A. Pérez-Torres, P. Pérez-González, J.-S. Huang, M. Davis, P. Guhathakurta, P. Barmby, C. J. Conselice, M. Lozano, J. A. Newman, and M. C. Cooper. Extragalactic background light inferred from AEGIS galaxy-SED-type fractions. *MNRAS*, 410:2556–2578, February 2011.

[26] S. A. Drake and A. P. Smale. The HEASARC in 2016: 25 Years and Counting. In *AAS/High Energy Astrophysics Division #15*, volume 15 of *AAS/High Energy Astrophysics Division*, page 116.16, April 2016.

[27] G. M. Dubner, A. J. Green, W. M. Goss, D. C.-J. Bock, and E. Giacani. Neutral Hydrogen in the Direction of the VELA Supernova Remnant. , 116:813–822, August 1998.

[28] Gloria Dubner and Elsa Giacani. Radio emission from supernova remnants. *Astronomy and Astrophysics Review*, 23:3, Sep 2015.

[29] A. R. Duncan, R. T. Stewart, R. F. Haynes, and K. L. Jones. The VELA supernova remnant and the GUM nebula: new perspectives at 2.4 GHz. *MNRAS*, 280:252–266, May 1996.

[30] J. Eagle, S. Marchesi, D. Castro, M. Ajello, L. Duvidovich, and L. Tibaldo. 2FHL J0826.14500: Discovery of a Possible ShockCloud Interaction on the Western Edge of the Vela Supernova Remnant. *ApJ*, 870:35, January 2019.

[31] S. E. S. Ferreira and O. C. de Jager. Supernova remnant evolution in non-uniform media. *International Cosmic Ray Conference*, 2:593–596, 2008.

[32] A. Fruscione, J. C. McDowell, G. E. Allen, N. S. Brickhouse, D. J. Burke, J. E. Davis, N. Durham, M. Elvis, E. C. Galle, D. E. Harris, D. P. Huenemoerder, J. C. Houck, B. Ishibashi, M. Karovska, F. Nicastro, M. S. Noble, M. A. Nowak, F. A. Primini, A. Siemiginowska, R. K. Smith, and M. Wise. CIAO: Chandra's data analysis system. In *Society of Photo-Optical Instrumentation Engineers (SPIE) Conference Series*, volume 6270 of , page 62701V, June 2006.

[33] S. Funk. Results from the H.E.S.S. Galactic Plane survey. *International Cosmic Ray Conference*, 4:123, 2005.

[34] H. E. S. S. Collaboration, H. Abdalla, A. Abramowski, F. Aharonian, F. A. Benkhali, A. G. Akhperjanian, T. Andersson, E. O. Angüner, M. Arrieta, P. Aubert, and et al. H.E.S.S. observations of RX J1713.7-3946 with improved angular and spectral resolution: Evidence for gamma-ray emission extending beyond the X-ray emitting shell. *A&A*, 612:A6, April 2018.

[35] H.E.S.S. Collaboration, H. Abdalla, A. Abramowski, F. Aharonian, F. Ait Benkhali, A. G. Akhperjanian, E. O. Angüner, M. Arakawa, M. Arrieta, P. Aubert, and et al. Deeper H.E.S.S. observations of Vela Junior (RX J0852.0-4622): Morphology studies and resolved spectroscopy. *A&A*, 612:A7, April 2018.

[36] H.E.S.S. Collaboration, H. Abdalla, A. Abramowski, F. Aharonian, F. A. Benkhali, E. O. Angüner, M. Arakawa, M. Arrieta, P. Aubert, M. Backes, and et al. The H.E.S.S. Galactic plane survey. *A&A*, 612:A1, April 2018.

[37] J. Holder, R. W. Atkins, H. M. Badran, G. Blaylock, S. M. Bradbury, J. H. Buckley, K. L. Byrum, D. A. Carter-Lewis, O. Celik, Y. C. K. Chow, P. Cogan, W. Cui, M. K. Daniel, I. de la Calle Perez, C. Dowdall, P. Dowkontt, C. Duke, A. D. Falcone, S. J. Fegan, J. P. Finley, P. Fortin, L. F. Fortson, K. Gibbs, G. Gillanders, O. J. Glidewell, J. Grube, K. J. Gutierrez, G. Gyuk, J. Hall, D. Hanna, E. Hays, D. Horan, S. B. Hughes, T. B. Humensky, A. Imran, I. Jung, P. Kaaret, G. E. Kenny, D. Kieda, J. Kildea, J. Knapp, H. Krawczynski, F. Krennrich, M. J. Lang, S. LeBohec, E. Linton, E. K. Little, G. Maier, H. Manseri, A. Milovanovic, P. Moriarty, R. Mukherjee, P. A. Ogden, R. A. Ong, D. Petry, J. S. Perkins, F. Pizlo, M. Pohl, J. Quinn, K. Ragan, P. T. Reynolds, E. T. Roache, H. J. Rose, M. Schroedter, G. H. Sembroski, G. Sleege, D. Steele, S. P. Swordy, A. Syson, J. A. Toner, L. Valcarcel, V. V. Vassiliev, S. P. Wakely, T. C. Weekes, R. J. White, D. A. Williams, and R. Wagner. The first VERITAS telescope. *Astroparticle Physics*, 25:391–401, July 2006.

[38] T. Kamae, N. Karlsson, T. Mizuno, T. Abe, and T. Koi. *Parameterization of γ, $e^{+/-}$, and Neutrino Spectra Produced by p-p Interaction in Astronomical Environments. ApJ*, 647:692–708, August 2006.

[39] O. Kargaltsev, B. Rangelov, and G. G. Pavlov. Gamma-ray and X-ray Properties of Pulsar Wind Nebulae and Unidentified Galactic TeV Sources. *ArXiv e-prints*, May 2013.

[40] A. Leccardi and S. Molendi. Radial temperature profiles for a large sample of galaxy clusters observed with XMM-Newton. *A&A*, 486:359–373, August 2008.

[41] F. J. Lu and B. Aschenbach. Spatially resolved X-ray spectroscopy of the Vela supernova remnant. *A&A*, 362:1083–1092, October 2000.

[42] D. H Lumb, N. Schartel, and F. A Jansen. XMM-Newton (X-Ray Mulit-Mirror Mission) Observatory. *ArXiv e-prints*, February 2012.

[43] M. A. Malkov, P. H. Diamond, and R. Z. Sagdeev. Mechanism for spectral break in cosmic ray proton spectrum of supernova remnant W44. *Nature Communications*, 2:194, February 2011.

[44] A. Manzali, A. de Luca, and P. A. Caraveo. Using XMM-Newton to measure the spectrum of the Vela pulsar and its phase variation. , 308:601–605, April 2007.

[45] R. Mewe, E. H. B. M. Gronenschild, and G. H. J. van den Oord. Calculated X-radiation from optically thin plasmas. V. , 62:197–254, November 1985.

[46] R. Mewe, J. R. Lemen, and G. H. J. van den Oord. Calculated X-radiation from optically thin plasmas. VI - Improved calculations for continuum emission and approximation formulae for nonrelativistic average Gaunt factors. , 65:511–536, September 1986.

[47] M. Mori. *Nuclear enhancement factor in calculation of Galactic diffuse gamma-rays: A new estimate with DPMJET-3. Astroparticle Physics*, 31:341–343, June 2009.

[48] Y. Moriguchi, N. Yamaguchi, T. Onishi, A. Mizuno, and Y. Fukui. A ^{12}CO (J = 1 – 0) Survey of Molecular Clouds toward the Vela Supernova Remnant with NANTEN. , 53:1025–1036, December 2001.

[49] T. Murphy, T. Mauch, A. Green, R. W. Hunstead, B. Piestrzynska, A. P. Kels, and P. Sztajer. The second epoch Molonglo Galactic Plane Survey: compact source catalogue. *MNRAS*, 382:382–392, November 2007.

[50] R. A. Ong. Highlights from VERITAS on VHE gamma-ray sources in our Galaxy. *Advances in Space Research*, 53:1483–1491, May 2014.

[51] M. Renaud. Latest results on Galactic sources as seen in VHE gamma-rays. *ArXiv e-prints*, May 2009.

[52] S. P. Reynolds. Supernova Remnants at High Energy. , 46:89–126, September 2008.

[53] P. Slane. *Pulsar Wind Nebulae*, page 2159. 2017.

[54] P. Slane, A. Bykov, D. C. Ellison, G. Dubner, and D. Castro. Supernova Remnants Interacting with Molecular Clouds: X-Ray and Gamma-Ray Signatures. , 188:187–210, May 2015.

[55] P. Slane, I. Lovchinsky, C. Kolb, S. L. Snowden, T. Temim, J. Blondin, F. Bocchino, M. Miceli, R. A. Chevalier, J. P. Hughes, D. J. Patnaude, and T. Gaetz. Investigating the Structure of Vela X. *ArXiv e-prints*, August 2018.

[56] K. J. van der Heyden, F. Paerels, J. Cottam, J. S. Kaastra, and G. Branduardi-Raymont. Detection of X-ray line emission from the shell of SNR B0540-69.3 with XMM-Newton RGS. *A&A*, 365:L254–L258, Jan 2001.

[57] W. Voges, B. Aschenbach, T. Boller, H. Bräuninger, U. Briel, W. Burkert, K. Dennerl, J. Englhauser, R. Gruber, F. Haberl, G. Hartner, G. Hasinger, M. Kürster, E. Pfeffermann, W. Pietsch, P. Predehl, C. Rosso, J. H. M. M. Schmitt, J. Trümper, and H. U. Zimmermann. The ROSAT all-sky survey bright source catalogue. *A&A*, 349:389–405, September 1999.

[58] Kurt W. Weiler and Richard A. Sramek. Supernovae and supernova remnants. *Annual Review of Astronomy and Astrophysics*, 26(1):295–341, 1988.

[59] P. F. Winkler, B. J. Williams, S. P. Reynolds, R. Petre, K. S. Long, S. Katsuda, and U. Hwang. A High-resolution X-Ray and Optical Study of SN 1006: Asymmetric Expansion and Small-scale Structure in a Type Ia Supernova Remnant. *ApJ*, 781:65, February 2014.